# Single-Cell Mass Spectrometry of Subpopulations Selected by Fluorescence Microscopy

Linwen Zhang,[†] Christopher J. Sevinsky,[‡] Brian M. Davis,[‡] and Akos Vertes*,[†]

[†]Department of Chemistry, The George Washington University, Washington, District of Columbia 20052, United States
[‡]GE Global Research, Niskayuna, New York 12309, United States

**S** *Supporting Information*

**ABSTRACT:** Specific subpopulations in a heterogeneous collection of cells, for example, cancer stem cells in a tumor, are often associated with biological or medical conditions. Fluorescence microscopy, based on biomarkers labeled with fluorescent probes, is a widely used technique for the visualization and selection of such cells. Phenotypic differences for these subpopulations at the molecular level can be identified by their untargeted analysis by single-cell mass spectrometry (MS). Here, we combine capillary microsampling MS with fluorescence microscopy for the analysis of metabolite and lipid levels in single cells to discern the heterogeneity of subpopulations corresponding to mitotic stages. The distributions of ATP, reduced glutathione (GSH), and UDP-*N*-acetylhexosamine (UDP-HexNAc) levels in mitosis reveal the presence of 2−3 underlying subpopulations. Cellular energy is found to be higher in metaphase compared to prometaphase and slightly declines in anaphase, telophase, and cytokinesis. The [GTP]/[GDP] ratio in cytokinesis is significantly higher than in prometaphase and anaphase. Pairwise correlations between metabolite levels show that some molecules within a group, including certain amino acids and nucleotide sugars, are strongly correlated throughout mitosis, but this is not related to their pathway distances. Correlations are observed between monophosphates (AMP and GMP), diphosphates (ADP and GDP), and triphosphates (ATP and GTP) of different nucleosides. In contrast, there is low correlation between diphosphates and triphosphates of the same nucleoside (ADP and ATP).
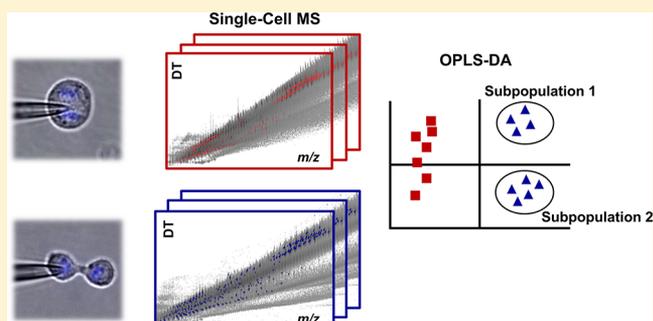
With the development of diverse affinity-based and genetically encoded fluorescent probes, cellular phenotypes and disease states can be identified to reveal cell-to-cell heterogeneity even within a seemingly homogeneous cell population.[1] For example, fluorescence microscopy has been applied for the visualization and analysis of mitotic phenotypes by labeling a component protein of the nucleosome, histone H2B.[2] Cells distinguished by the fluorescent probes can also be sorted into more homogeneous groups by flow cytometry.[3,4] Mass cytometry is a high-throughput technique that allows the distinction of cellular subpopulations by use of over 40 protein markers labeled with metal probes for detection by inductively coupled plasma mass spectrometry (ICP-MS).[5] These probes, however, only report on the presence or absence of a particular molecular feature or receptor and do not provide information on the metabolite and lipid composition of the corresponding cells.

Transcriptomic, proteomic, and metabolomic heterogeneity of cell populations can be classified into two main subtypes. First, there are populations where two or more subpopulations exist; for example, the presence or absence of a certain enzyme due to genetic mutations can result in high or low levels of metabolic products. Second, even in the absence of subpopulations, transcript, protein, and metabolite levels exhibit stochastic variations. The magnitudes of such variations are linked to the regulatory networks in the cell and can be expressed as, for example, metabolic noise.[6,7]

To investigate these two types of metabolic heterogeneity with higher molecular coverage, a number of advanced MS techniques have been developed for the untargeted analysis of hundreds of metabolites and lipids from single cells.[8−11] Secondary ion mass spectrometry (SIMS)[12] and matrix-assisted laser desorption ionization (MALDI)-MS[13,14] have been applied for single-cell analysis under vacuum conditions. A recent highly relevant paper reports on selecting cells via fluorescent imaging for single-cell MALDI-MS followed by capillary electrophoresis−electrospray ionization (ESI)-MS analysis.[15] Ambient methods, such as laser ablation electrospray ionization (LAESI)-MS,[16,17] live single-cell MS,[18,19] and single-probe MS,[20] have been developed for metabolic analysis of single cells or organelles in their native environment.

Recently, we have developed capillary microsampling ESI-MS with ion mobility separation (IMS) for metabolic and lipidomic analysis of single plant[21] and mammalian cells.[10]

Characteristics of cellular physiological states, for example, adenylate energy charge (AEC), and their heterogeneity in cell populations affected by xenobiotics were revealed by this technique. Activation of metabolic pathways in specialized cellular phenotypes was also detected at the single-cell level. In these studies, however, phenotypic differences were either detected on the basis of cell morphology or induced by a chemical.

To investigate more subtle metabolic differences between cells, fluorescence labeling of cellular states can be introduced. For example, mitotic stages in cell division can be distinguished by labeling the nuclear DNA with a fluorescent dye and observing the changes in configuration of the chromosomes. Mitotic stages, such as prometaphase, metaphase, anaphase, and telophase, together with cytokinesis, can be clearly visualized and differentiated in live cells.[2,22,23] In a previous study, fluctuations of ATP levels in single cells during mitosis were monitored by a fluorescence probe.[24] Fluorescence probes can only differentiate cells on the basis of a predetermined selection of labels. By integrating fluorescence microscopy with single-cell MS analysis, some cell subpopulations can be preidentified, and the molecular phenotypes and heterogeneity within the corresponding subpopulation can be analyzed by single-cell MS. Integration of the two techniques provides information on global metabolite levels and reveals phenotypic differences within the population and their heterogeneity within a subpopulation of cells (metabolic noise). This approach can be potentially applied for single-cell analysis of diverse biological systems prelabeled with fluorescent probes, such as stem cells,[25] glial cells,[26] and cancer cells,[27] to gain new information on cell phenotypes and the heterogeneity within the subpopulations without the need for further labeling.

In this study, the combination of fluorescence microscopy and capillary microsampling ESI-IMS-MS is used to differentiate and selectively analyze individual hepatocellular carcinoma cells in distinct mitotic stages. The changes of relative metabolite levels, cellular heterogeneity, and metabolic noise are investigated in dividing cells and in cytokinesis.

## ■ EXPERIMENTAL SECTION

**Chemicals.** HPLC-grade methanol and water, $DiOC_6(3)$ (D273), Hoechst 33342 (H1399), and RNase A (EN0531) were purchased from Thermo Fisher Scientific (Waltham, MA). Hoechst 33342 stock solution was made by dissolving it in autoclaved water at 1 mg/mL concentration. Nocodazole (M1404, ≥99% purity), dimethyl sulfoxide (DMSO; D2650), Triton X-100 (T9284), and propidium iodide (P4864) were purchased from Sigma−Aldrich (St. Louis, MO). Paraformaldehyde (15710) was obtained from Electron Microscopy Sciences (Hatfield, PA). Nocodazole stock solution was prepared in DMSO at a concentration of 100 μg/mL.

**Cell Culture and Fluorescence Microscopy.** HepG2/C3A cells were obtained from the American Type Culture Collection (ATCC, Manassas, VA, CRL-10741). Cells were maintained in Eagle's minimum essential medium (30-2003, ATCC, Manassas, VA) supplemented with 10% fetal bovine serum (30-2020, ATCC, Manassas, VA) and 1% penicillin−streptomycin (15070063, Invitrogen, Grand Island, NY). Cells were seeded on a 35 mm culture dish (Corning, Tewksbury, MA) filled with 2 mL of medium at a density of $2 \times 10^5$ cells/mL for 24 h before drug treatment. To arrest the cell cycle at the G2/M phase, cells were treated with nocodazole at a concentration of 100 ng/mL for 12 h. After 12 h treatment,

cells were washed three times with fresh medium and released from arrest by keeping them in regular culture medium for 1 h. To identify the mitotic stages, cellular double-stranded DNA (dsDNA) was stained with 0.1 μg/mL Hoechst 33342 for 5 min. The endoplasmic reticulum was counterstained by $DiOC_6(3)$ for imaging purposes. Fluorescence microscopic images were obtained by an inverted microscope (IX71, Olympus, Tokyo, Japan) equipped with a scientific-grade complementary metal−oxide semiconductor (sCMOS) camera (Orca-Flash 4.0 V2, Hamamatsu, Hamamatsu City, Japan).

**Flow Cytometry.** HepG2/C3A cells were treated with 100 ng/mL nocodazole or vehicle control (0.1% DMSO) or left untreated for 24 h prior to flow cytometry. Cells were fixed with ice-cold 70% ethanol for 30 min and then were resuspended in 50 μL of phosphate-buffered saline (PBS) with 100 μg/mL RNase A. Cells were treated with 200 μL of 50 μg/mL propidium iodide, and 20 000 events were analyzed on a flow cytometer (FC500, Beckman Coulter Life Sciences, Indianapolis, IN).

**Confocal Immunofluorescence Microscopy.** HepG2/C3A cells were plated onto glass coverslips, cultured overnight, and then treated with 100 ng/mL nocodazole or vehicle control for 24 h. Cells were fixed in 4% paraformaldehyde and permeabilized in 0.1% Triton X-100. Cells were stained with mouse monoclonal antibody against α-tubulin (3873, Cell Signaling Technology, Danvers, MA) and rabbit polyclonal antibody against phosphohistone H3 (9701, Cell Signaling Technology, Danvers, MA), followed by detection with Cy3- and Cy5-labeled secondary antibodies (Jackson ImmunoResearch Laboratories, Inc., West Grove, PA) and 4,6-diamidino-2-phenylindole (DAPI; Sigma−Aldrich, St. Louis, MO). Images were acquired by use of a confocal microscope (LSM880, Carl Zeiss Microscopy, Thornwood, NY) using a 100× objective with the Airyscan super-resolution detector.

**Wide-Field Immunofluorescence Microscopy.** HepG2/C3A cells were plated onto black-well 96-well plates (Corning Inc., Corning, NY) overnight and then treated with 100 ng/mL nocodazole or vehicle control for 24 h. The cells were fixed in 4% paraformaldehyde, permeabilized with 0.1% Triton X-100, and stained with a mouse monoclonal antibody against α-tubulin (Cell Signaling Technology 3873) or rabbit monoclonal antibody against β-tubulin (Cell Signaling Technology 2128), followed by detection with Cy3-labeled secondary antibodies (Jackson ImmunoResearch Laboratories, Inc., West Grove, PA) and DAPI (Sigma−Aldrich, St. Louis, MO). Images were acquired by use of an IN Cell Analyzer 2000 (GE Healthcare Life Sciences, Pittsburgh, PA). Image thresholding and analysis was performed with the algorithm of Otsu[28] in ImageJ image analysis software,[29] and average tubulin expression levels were quantified for each sample.

**Capillary Microsampling Electrospray Ionization Ion Mobility Separation Mass Spectrometry.** The experimental procedures for capillary microsampling ESI-IMS-MS were described in detail in a previous publication.[10] Briefly, microsampling glass capillaries (TW100F-3, World Precision Instruments, Sarasota, FL) were pulled by a micropipette puller (P-1000, Sutter Instrument Co., Novato, CA) to produce sharp tips with ∼1 μm openings. The pulled capillary was attached to a capillary holder (IM-H1, Narishige, Tokyo, Japan) and the capillary holder was mounted on a micromanipulator (TransferMan NK2, Eppendorf, Hauppauge, NY) on the inverted microscope.
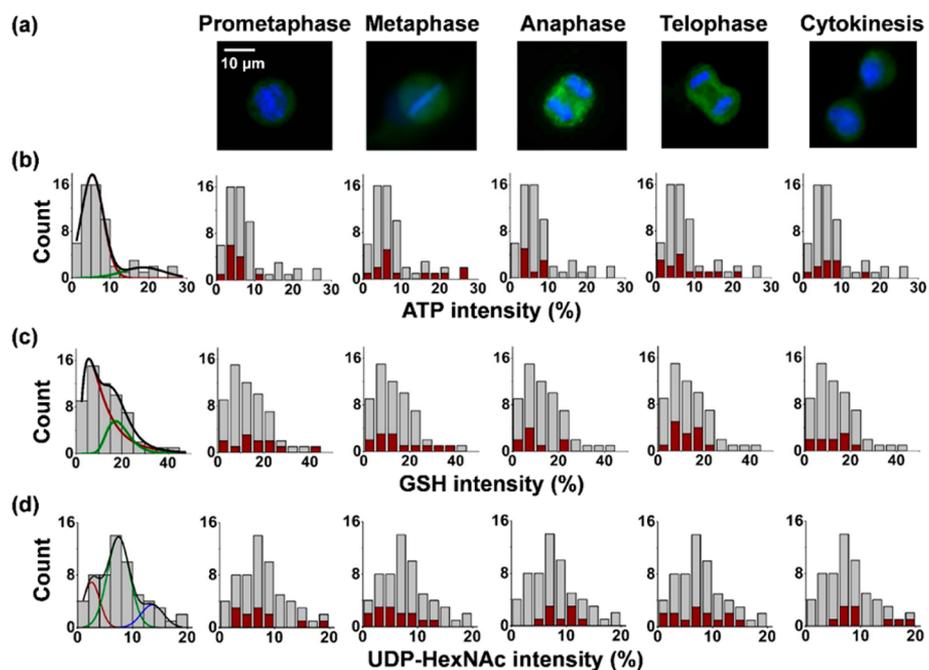
**Figure 1.** (a) Fluorescence microscopic images of cells at distinct mitotic stages. Cellular DNA was stained by Hoechst 33342 (blue), and the endoplasmic reticulum was counterstained by $DiOC_6(3)$ (green). (b−d) Distributions of normalized ion intensities for (b) ATP, (c) GSH, and (d) UDP-HexNAc in the entire mitotic cell population (gray bars) and in cells in different mitotic stages (red bars). (b) The distribution of ATP intensities for the mitotic cells is deconvoluted into two normal distributions shown in green and red, with the cumulative curve in black. (c) The distribution of GSH intensities is deconvoluted into two log-normal distributions shown in red and green, with the cumulative curve marked by black. (d) The distribution of UDP-HexNAc levels is deconvoluted into three normal distributions shown in red, green, and blue. The cumulative curve is shown in black.

After staining by Hoechst 33342, cells were washed with fresh culture medium. The dish was finally filled with 0.5 mL of medium before sampling. The dish containing adherent cells was placed on the microscope stage, and the cells of interest were located in bright-field mode to avoid photodamage due to the UV excitation needed for fluorescence. To determine the particular mitotic stages for the cells, fluorescence microscopy was used. A filter cube (49000, Chroma, Bellows Falls, VT) that supports emission wavelengths in the 417−477 nm range and excitation wavelengths in the 352−402 nm range was installed to visualize the stained DNA. To minimize cell damage by the intense UV radiation applied for excitation, a neutral density filter was inserted (32ND50, Olympus, Tokyo, Japan) and the exposure time was limited to ∼5 s by quickly switching between bright-field and fluorescent modes. Once the mitotic stage of the selected cell was determined, the sampling capillary tip was inserted and negative pressure was applied by a syringe to extract cell contents. A microscopic image of a capillary tip after sampling a cell is shown in Figure S2. The average sampled cell volume was calculated to be ∼0.2 pL from the geometry of the capillary tip. The sampled volume showed variations between 0.1 and 0.3 pL. To minimize the bias from differences in sampled volume, volume-independent ion intensity ratios (ratiometric indicators) were compared for the different mitotic stages. In other cases, ion intensities were normalized by the sum of sample related ion intensities, which also reduced the dependence on sample volume.

After microsampling, the capillary was backfilled with 1.0 μL of electrospray solution (80% methanol) and a platinum wire was inserted to establish contact with the liquid. The capillary tip was placed ∼5 mm away from the inlet orifice of the mass spectrometer (Synapt G2-S, Waters Co., Milford, MA). High voltage (−2000 V) was applied to the wire by a regulated power supply (PS350, Stanford Research Systems, Sunnyvale, CA) to establish a stable electrospray. Cell-related ions were produced for ∼5 s at the beginning of each measurement, and the electrospray background signal was acquired for another ∼20 s. The ions were separated by a traveling-wave ion mobility system on the basis of their collision cross sections (CCS) and analyzed by a high-performance time-of-flight (TOF) mass spectrometer according to their mass-to-charge ratios ($m/z$). The ions entered the trap and transfer cells with 4.0 and 2.0 eV kinetic energies, respectively. To enhance identification of the detected ions, tandem MS was performed on cell lysate samples by collision-induced dissociation with collision energies between 20 and 30 eV.

**Data Analysis.** A three-dimensional data set, with ion intensity as a function of drift time (DT) and $m/z$, was acquired for each measurement and the corresponding DT versus $m/z$ plot was visualized by DriftScope 2.8 (Waters Co., Milford, MA) software. The CCS values for the ions were derived from their DTs by DriftScope 2.8 with a polyalanine oligomer mixture ($n = 4−14$) as the calibrant. The mass spectra integrated over all DTs within the $m/z$ range of 20−700 were processed by MassLynx 4.1 (Waters Co., Milford, MA), and the electrospray and PBS background was subtracted. The processed mass spectra were exported to mMass software[30] for peak picking and deisotoping, followed by subtraction of the interfering ions from the medium. For statistical analysis, the generated lists of $m/z$ and intensity values from mMass were imported into MetaboAnalyst 3.0.[31] Ion abundances were normalized to the sum of peak intensities in each spectrum, and volcano plots were generated to find ions with significant differences between the mitotic stages.
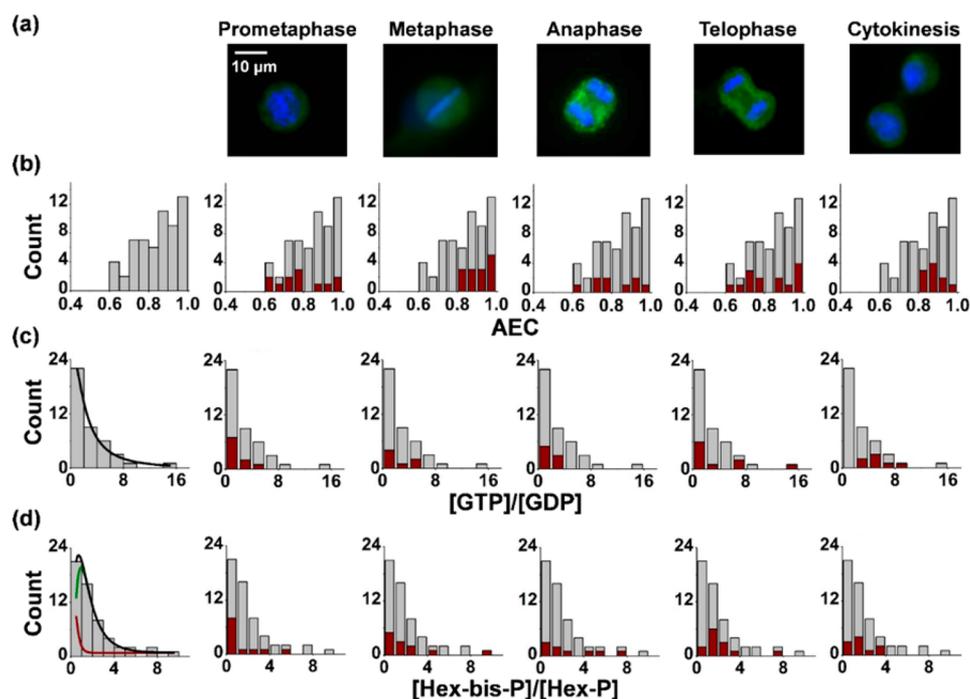
**Figure 2.** (a) Fluorescence microscopic images of cells at distinct mitotic stages. (b−d) Distributions of (b) AEC, (c) [GTP]/[GDP], and (d) [Hex-bis-P]/[Hex-P] ratios for the entire mitotic population (gray bars) and for cells in different mitotic stages (red bars). The distribution of [GTP]/[GDP] ratio is fitted by a log-normal distribution. The [Hex-bis-P]/[Hex-P] ratio is deconvoluted into two log-normal distributions shown in red and green, with the cumulative curve in black.

Tentative metabolite assignments were based on accurate mass and CCS values and searches in the Human Metabolome Database (http://www.hmdb.ca/) and the METLIN metabolite database (https://metlin.scripps.edu/) with a mass window of 20 mDa. The assigned metabolites were confirmed by tandem MS.

## RESULTS AND DISCUSSION

**Analysis of Single Cells in Different Mitotic Stages.** On the basis of distinct chromosome morphologies, 59 individual cells were selected and identified as being in prometaphase, metaphase, anaphase, telophase, or cytokinesis. Figure 1a shows merged fluorescence microscopic images of the distributions of chromosomes and chromatids within the cells in different mitotic stages. The corresponding fluorescence microscopic images before merging and detailed descriptions are provided in Figure S3. For each stage, single-cell mass spectra of 9−14 cells were obtained by capillary microsampling ESI-IMS-MS. After ion subtraction from ESI and PBS background and deisotoping, ~100 cell-related ions remained in the spectra. Representative mass spectra for cells in different mitotic stages are shown in Figure S4. On the basis of a combination of accurate masses, collision cross sections, and collision-induced dissociation-based fragmentation patterns, 29 metabolites and 54 lipids (see Tables S1 and S2) were assigned in the spectra. The reference CCS values were obtained from previous publications.[32,33] Ion assignments were confirmed by tandem MS, except for CDP-ethanolamine, which was assigned on the basis of accurate mass measurement alone. Examples of tandem mass spectra for metabolite assignments are shown in Figure S5. The tandem MS fragments for lipid ion assignments are listed in Table S2. The assigned metabolites mainly included amino acids, nucleotides, and nucleotide sugars. These

identifications expanded our previous single-cell results and provided more extensive molecular coverage for hepatocytes.[10]

The intensities of the ions in ESI mass spectra are known to be affected by the presence of in-source fragmentation and structural isomers.[34] Detailed discussion of the types of fragmentations and isomers applicable to our spectra, and the related intensity corrections, are presented in the Supporting Information (see Figure S6). To eliminate variations due to differences in sampled volumes, normalized ion abundances or ratiometric indicators were used to characterize the changes in cell physiological states throughout mitosis. A list of sample-related $m/z$ and abundance values for each cell was obtained by subtracting the ESI background from the cell spectra, followed by deisotoping by use of the mMass software.[30] Normalization was based on the sum of intensities for all sample-related ions, whereas ratiometric indicators were calculated for metabolically related species. Histogram distributions or box-and-whisker plots for normalized ion abundances and ratiometric indicators throughout mitosis are presented in Figures 1−4.

**Metabolite Distributions for Mitotic Cells and Individual Mitotic Stages.** Distributions of normalized intensities for ATP, reduced glutathione (GSH), and UDP-N-acetylhexosamine (UDP-HexNAc) for the entire mitotic population of synchronized cells are shown by gray bars, and those for the mitotic stages are presented by red bars in Figure 1panels b, c, and d, respectively. They exhibit specific features (i.e., shoulders and tails) that are indicative of underlying subpopulations. The distribution of ATP intensities shows a symmetric maximum at low values and a long tail. It is deconvoluted into a combination of two normal distributions shown in red and green (see the leftmost panel in Figure 1b) with medians at 5.3% ± 0.2% and 18.6% ± 3.4%, respectively. The corresponding cumulative curve is shown in black (adjusted $R^2$ = 0.96). Compared to the other three stages, the ATP abundances in prometaphase,

anaphase, and cytokinesis show narrower distributions and only contribute to the high-count low-intensity subpopulation marked by the red line (see the leftmost panel in Figure 1b). The ATP intensities in metaphase and telophase contribute to both the low- and high-median subpopulations. In fact, the high-median subpopulation (green line) originates exclusively from these two stages. To statistically identify cell subpopulations in different mitotic stages, orthogonal partial least-squares discriminant analysis (OPLS-DA) was performed on the mass spectra. In Figure S7, the OPLS-DA scatter plot shows clear distinctions of the metabolite compositions between prometaphase and metaphase. In cells at metaphase, subpopulations corresponding to high (>10%) and low (≤10%) ATP levels are distinguished and highlighted in ellipses. This result is consistent with the ATP level distributions shown in Figure 1b.

Multiple efforts to use a combination of normal distributions to fit the overall GSH distribution in the leftmost panel of Figure 1c gave unsatisfactory results. This distribution is best fitted by the combination of two log-normal curves (shown in red and green) with the medians at 9.6% ± 2.2% and 18.5% ± 1.0%, respectively. The cumulative curve is presented in black (adjusted $R^2$ = 0.90). All five subpopulations contribute to the red curve with low median. The distribution with higher median (green line) reflects contributions from telophase, and to a lesser degree, anaphase and cytokinesis.

In Figure 1d, the UDP-HexNAc intensity distribution is deconvoluted into a combination of three normal distributions, shown in red, blue, and green, producing a cumulative curve depicted in black (adjusted $R^2$ = 0.90). The medians for the component curves are 2.5% ± 0.5%, 7.5% ± 0.3%, and 13.6% ± 1.0%, respectively. The presence of these underlying distributions is indicative of cell subpopulations that contain different levels of these metabolites. In Figure 1d, the distributions of UDP-HexNAc intensities in prometaphase and telophase contribute to all three deconvoluted subpopulations. In metaphase, the UDP-HexNAc intensities significantly contribute to the first and, to a lesser degree, the second subpopulation, represented by the red and green lines, respectively. In anaphase, the distribution for the normalized UDP-HexNAc intensity exhibits a narrower distribution than in the other stages, and it mostly contributes to the subpopulation with an intermediate median marked by the green line. The UDP-HexNAc intensities in cytokinesis contribute to the subpopulations with intermediate and high medians, marked by the green and blue lines, respectively.

Figure 2 shows the distributions of three ratiometric indicators—AEC, [GTP]/[GDP], and [Hex-bis-P]/[Hex-P]—for the entire mitotic population (gray bars), and for the mitotic stages (red bars). The most commonly used indicator, AEC = ([ATP] + 0.5[ADP])/([ATP] + [ADP] + [AMP]), reflects the cellular energy stored in the adenylate pools on a scale of 0 to 1. For values of AEC > ∼0.8, the cell functions normally, whereas AEC < ∼0.5 can signal a major energy deficit, typically resulting in cell death. Figure 2b shows the overall distribution of AEC for the mitotic cells (gray bars) exhibiting a range of 0.60 < AEC < 1.00, indicating that the cells have sufficient energy for normal functioning. Compared to prometaphase, anaphase, and telophase, the AEC levels in metaphase and cytokinesis show significantly narrower distributions (see Figure 2b and the statistical ranges in Table S4a) centered on medians of 0.93 and 0.87, respectively. In a previous study, bulk analysis of HepG2 cells by HPLC showed

AEC = 0.81 ± 0.01,[35] a value fairly similar to our single-cell data.

Other significant ratios include [GTP]/[GDP] and [Hex-bis-P]/[Hex-P]; their distributions for the entire mitotic population are plotted in Figure 2panels c and d, respectively (gray bars). Here Hex-bis-P stands for hexose bisphosphate, and Hex-P denotes hexose phosphate. The distributions of these ratios are significantly skewed. The [GTP]/[GDP] and [Hex-bis-P]/[Hex-P] distributions can be characterized by one and two log-normal distributions (adjusted $R^2$ = 0.98 for both), respectively, indicating the potential presence of two subpopulations in the latter. In Figure 2c, the distributions of [GTP]/[GDP] ratios for mitotic stages are shifted to higher levels in cytokinesis compared to the earlier stages. The distributions of the [Hex-bis-P]/[Hex-P] ratio exhibit long tails for higher values. Compared to the two deconvoluted subpopulations in the first panel of Figure 2d, the prometaphase distribution is similar to the distribution with low ratios (red line). Part of the metaphase distribution also contributes to this subpopulation, but it also adds to the other subset of cells with higher [Hex-bis-P]/[Hex-P] ratios (green line in the first panel of Figure 2d). Cells in the remaining three stages mostly contribute to the latter subpopulation.

**Identification of Up- and Downregulated Metabolites.** A volcano plot is a two-dimensional scatter plot that connects statistical significance $[-\log_{10}(p)]$ with fold change values $[\log_2(\text{FC})]$, which is often used to identify significant changes between two groups of data sets. To identify significant abundance FC values between mitotic stages, volcano plots are constructed on the basis of pairwise comparisons of corresponding spectra by use of statistical significance, $p$, based on $t$-tests. The ion intensities, $I_{ik}$ for cell $i$ and ion type $k$, are normalized to the sum of the cell-related peak intensities in each spectrum followed by Pareto scaling that is defined as

$$\tilde{I}_{ik} = \frac{I_{ik} - \overline{I}_k}{\sqrt{s_k}}$$

where $\overline{I}_k$ is the mean of the intensities of a metabolite ion for all cells and $s_k$ is its standard deviation. The normalized metabolite abundance data for all cells is shown in Figure S8. Based on this, the fold change, $\text{FC}_k$, for ion $k$ between, for example, anaphase and metaphase is expressed as

$$\text{FC}_k = \frac{\langle \tilde{I}_{ik} \rangle_{\text{meta}}}{\langle \tilde{I}_{ik} \rangle_{\text{ana}}}$$

In Figure S9, the volcano plots show $\log_{10}(p)$ as a function of $\log_2(\text{FC})$ for the ions compared in prometaphase versus metaphase (panel a) and metaphase versus anaphase (panel b). The metabolite species that exhibit reduced (green symbols) or elevated (red symbols) levels are selected on the basis of FC values (FC ≤ 1/1.5 or FC ≥ 1.5, respectively) and a statistical significance of $p < 0.1$. Comparison of prometaphase and metaphase in Figure S9a reveals that ATP and UTP show higher abundances and AMP exhibits lower levels for the cells in metaphase. Compared to metaphase, cells in anaphase show lower levels of ATP and GSH and higher abundances of UDP-HexNAc and NAD$^+$ (see Figure S9b).

The medians, ranges, means, standard deviations, and normalities for the intensities of ATP, GSH, and UDP-HexNAc, normalized by the sum of all cell-related ion intensities, are shown in Table S3 sections a, b, and c, respectively. These data are visualized in Figure 3b–d as box-
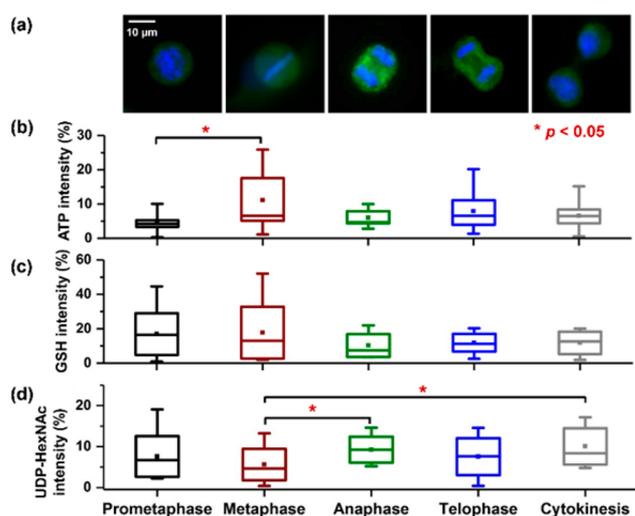
**Figure 3.** (a) Fluorescence microscopic images of cells at distinct mitotic stages. (b–d) Box-and-whisker plots for normalized (b) ATP, (c) GSH, and (d) UDP-HexNAc intensities from single cells at different mitotic stages.

and-whisker plots. To find significantly different metabolite levels in distinct mitotic stages, two-sampled $t$-test is performed for normally distributed data, whereas Mann–Whitney $U$-test is applied for non-normally distributed data (http://www.socscistatistics.com/tests/mannwhitney/, last accessed on 11/30/2017).

Table S3a and Figure 3b show normalized ATP intensity data for the five mitotic stages. The median of the normalized ATP intensity in metaphase is found to be elevated with more than 95% likelihood compared to prometaphase ($p < 0.05$ based on the Mann–Whitney $U$-test). The statistical ranges of ATP intensity in metaphase, telophase, and cytokinesis are 24.8%, 18.8%, and 14.6%, respectively, indicating wider distributions compared to other stages. Table S3b and Figure 3c show normalized GSH intensities for the five stages of mitosis. Consistent with Figure S9b, the median of normalized GSH intensity is decreased from 13.0% in metaphase to 7.4% in anaphase. The measured statistical ranges of GSH intensity show higher levels in prometaphase (43.7%) and metaphase (50.1%) compared to the other three stages.

In Table S3c and Figure 3d, normalized UDP-HexNAc intensities are presented for the mitotic stages. The data indicate that UDP-HexNAc levels are significantly elevated in anaphase and cytokinesis compared to metaphase. Levels of UDP-$N$-acetylglucosamine (UDP-GlcNAc), a glycosyl donor for the post-translational modification of nuclear and cytoplasmic proteins at specific serine or threonine residues by O-linked $\beta$-$N$-acetylglucosamine (O-GlcNAc) catalyzed by $\beta$-$N$-acetylglucosaminyltransferase (O-GlcNAc transferase, OGT), are known to be correlated with histone H3 modification that plays a significant role in cell cycle progression.[36]

A previous study showed that, between metaphase and telophase, the location of OGT within the dividing cell moved from the spindle pole to the midbody, whereas O-GlcNAc-modified proteins showed increased levels at the midbody and the nuclear membrane.[37] In Figure 1d, among the three subpopulations of UDP-HexNAc intensities, the distribution in metaphase significantly contributes to the low-intensity subpopulation; however, the distribution in anaphase mainly

contributes to the subpopulation with an intermediate UDP-HexNAc level. In Figure 3d, the median for normalized UDP-HexNAc intensity is increased from 4.6% in metaphase to 9.3% in anaphase ($p = 0.03$ based on $t$-test), and to 8.4% in cytokinesis ($p = 0.02$ based on $t$-test). When metaphase and telophase are compared, the median shows an increase from 4.6% to 7.8%. This finding is consistent with the increased level of protein O-GlcNAcylation in the developing nuclear membranes observed in telophase.

**Changes in Ratiometric Indicators throughout Mitotic Stages.** Certain biological processes are regulated by the abundance ratios of selected metabolite pairs. The collected data enable us to determine changes in the cellular heterogeneity of some ratiometric indicators. In particular, changes in the available cellular energy and microtubule polymerization dynamics during mitotic stages are explored. The median, statistical range, mean, standard deviation values, and normality for AEC, [GTP]/[GDP], and [Hex-bis-P]/[Hex-P] ratios are listed in Table S4 sections a, b and c, respectively. Data for AEC, [GTP]/[GDP] and [Hex-bis-P]/[Hex-P] are presented in Figure 4b–d as box-and-whisker plots.
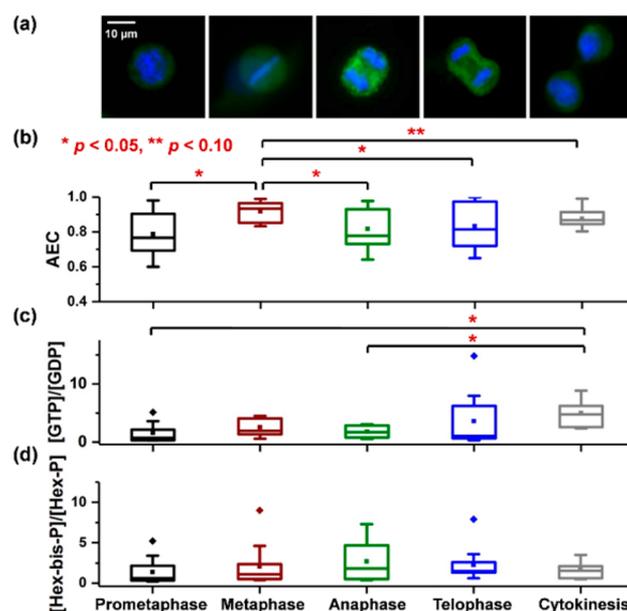


**Figure 4.** (a) Fluorescence microscopic images of cells at distinct mitotic stages. (b–d) Box-and-whisker plots for (b) AEC, (c) [GTP]/[GDP], and (d) [Hex-bis-P]/[Hex-P] ratiometric indicators in single cells at different mitotic stages.

Table S4a and the corresponding box-and-whisker plot in Figure 4b indicate that the median for AEC is increased from 0.77 in prometaphase to 0.93 in metaphase (with $p = 0.005$ based on $t$-test). Following metaphase, the median AEC level declines to 0.78 ($p = 0.04$) in anaphase, 0.82 ($p = 0.04$) in telophase, and 0.87 ($p = 0.09$) in cytokinesis. The ranges for metaphase and cytokinesis are significantly narrower compared to the other three stages. All the AEC distributions, except for the overall distribution, satisfy the normality test.

AMP-activated protein kinase (AMPK) is an enzyme that senses cellular energy states through the competitive binding of ATP versus AMP or ADP to the $\gamma$-subunit of AMPK for maintaining cellular energy homeostasis.[38,39] Activation of

AMPK induced by elevated cellular AMP and ADP levels leads to increased ATP production and reduced ATP consumption through complex regulation of metabolic pathways.[40] In our study, the lower AEC = 0.77 (see Table S4a) and ATP intensity (4.2% in Table S3a) medians in prometaphase compared to AEC = 0.93 and ATP intensity (6.6%) in metaphase are likely accompanied by activated AMPK in the mitotic arrest induced by nocodazole. Consistent with this hypothesis, the distribution of ATP abundances in prometaphase almost exclusively contributes to the subpopulation with low median level. However, the distribution of ATP levels in metaphase exhibits a long tail overlapping the second subpopulation with a higher median (see Figure 1b). This is consistent with the significantly higher overall ATP levels in metaphase compared to prometaphase (see Figure 3b).

An alternative explanation of these differences is the selective transition of cells with higher AEC from prometaphase to metaphase. Due to the ATP requirement for releasing cells from prometaphase, a fraction of the cells with lower AEC levels (0.60 < AEC < 0.83) might not be able to enter metaphase. This can result in the observed decrease of the statistical range from 0.38 in prometaphase to 0.16 in metaphase.

Other studies have shown that ATP is required for releasing the cells from the mitotic checkpoint between metaphase and anaphase.[41,42] The decrease of the median from AEC = 0.93 in metaphase to AEC = 0.78 in anaphase might be due to consumption of ATP during this process. The increase of statistical range from 0.16 in metaphase to 0.34 in anaphase reflects the heterogeneity of energy requirements and ATP consumption for, as an example, the breakup of the mitotic checkpoint complex.[41] This is also reflected in the distribution of ATP levels in anaphase that lacks cells with high ATP levels and only contributes to the low-intensity subpopulation.

Another ratiometric indicator, the [GTP]/[GDP] ratio, is known to regulate microtubule polymerization dynamics.[43] As our [GTP]/[GDP] ratio data for prometaphase and telophase do not satisfy normality, the Mann−Whitney U-test was used to establish statistically significant differences in comparisons involving these stages. Although the median value for the [GTP]/[GDP] ratio is increased from 0.7 to 1.9 between prometaphase and metaphase (see Table S4b), statistically significant change cannot be established due to the large and overlapping ranges. The [GTP]/[GDP] ratios show significant differences between prometaphase and cytokinesis ($p < 0.05$ for the Mann−Whitney U-test) and between anaphase and cytokinesis ($p = 0.01$ for the t-test). Compared to the medians, the ranges for the [GTP]/[GDP] ratios are wide, indicating broad distributions for all stages.

During cell division, the mitotic spindle is mainly composed of microtubules that participate in the alignment and separation of chromosomes. As microtubule polymerization is affected by the [GTP]/[GDP] ratio in the cell, one can link changes in this ratio to the formation and degradation of mitotic spindles. If the GTP consumed in microtubule polymerization is a significant part of the cellular GTP pool, the formation of spindles in prometaphase lowers the [GTP]/[GDP] ratio. This is consistent with the low [GTP]/[GDP] median observed for prometaphase (see Table S4b). Conversely, during the degradation of spindles in telophase, microtubules are depolymerized; that is, less GTP is used for polymerization, resulting in higher [GTP]/[GDP] ratios in the cells during cytokinesis (see Table S4b).

The [Hex bis-P]/[Hex-P] ratios are known to affect multiple metabolic pathways, including important roles in glycolysis and the pentose phosphate pathway. The chemical structures of hexose phosphate and hexose bisphosphate cannot be further specified by our current methods. Here, we consider hexose phosphate to represent the sum of glucose phosphates and fructose phosphates, whereas hexose bisphosphate corresponds to fructose bisphosphate, the dominant form compared to glucose bisphosphate. Comparison of the [Hex-bis-P]/[Hex-P] ratios in single cells in different mitotic stages by the Mann−Whitney U-test shows no significant differences are found ($p < 0.05$) in their medians and ranges (see Table S4c).

As a means of verification, the medians for [Hex-bis-P]/[Hex-P] ratios measured for single mitotic cells are compared to data for large cell populations. In a previous study, [fructose 1,6-bisphosphate]/[Hex-P] = 1.42 was found in $\sim 10^6$ iBMK cells by conventional metabolomics techniques.[44] The medians for [Hex-bis-P]/[Hex-P] ratios for different mitotic stages ranged between 0.6 and 1.8, bracketing the value obtained for large cell populations.

To characterize the technical variance, a standard mixture of glutamate and glucose 6-phosphate solutions was analyzed by the technique used for single-cell measurements. Twenty replicates for the [glutamate]/[glucose 6-phosphate] ratio were measured, yielding a technical variance of $\sim 17\%$ relative standard deviation (RSD). The corresponding cellular measurements showed an RSD of $\sim 40\%$, which indicated that the technical variance was much lower than the combination of technical and biological variances.

**Pairwise Correlation Analysis of Metabolite Abundances.** To explore potential correlations between the abundances of the assigned metabolites throughout the mitotic stages, Pearson correlation analysis was performed. In the low mass range ($50 < m/z < 670$) of the 59 mass spectra corresponding to single cells, 40 independent deisotoped peaks can be found. The $40 \times 40$ coefficient matrix resulting from the correlation analysis is shown in Figure S10 in order of increasing $m/z$ values. For visualization, the cells are colored on a graded scale from −1.00 (corresponding to the darkest blue) to 0.00 (representing the midpoint with white) to +1.00 (corresponding to the darkest red). The correlation coefficients, $r_{ij}$, and the $-\log(p)$ values expressing their t-test-based significance for ions and ionic fragments with $r_{ij} > 0.55$ are listed in Table S5.

Correlations in ion intensities for the 59 cells stem from two different sources. Some correlations are the result of instrumental effects. In this category, we observe the fragments of UDP-hexose and UDP-HexNAc being strongly correlated with $r_{ij} > 0.90$. More interestingly, some metabolite intensities vary together due to biological reasons. For example, UDP-hexose and UDP-HexNAc, and leucine/isoleucine and glutamine, exhibit strong correlations with coefficients of $r_{ij} = 0.89$ and 0.83, respectively (see Table S5) and probably fall into this category.

Previous studies show that in large cell populations exposed to stress, the transcript−transcript and metabolite−metabolite correlations are inversely related to their pathway distances.[45−48] Our results show that some molecules similar in nature, including certain amino acids, such as glutamine and glutamate, and nucleotide sugars, such as UDP-hexose and UDP-HexNAc, are strongly correlated, but this does not seem to be related to their pathway distances. Interesting correlations ($r_{ij} > 0.55$) are observed between monophosphates (AMP and

GMP), diphosphates (ADP and GDP), and triphosphates (ATP and GTP) of different nucleosides. In contrast, there is low correlation between diphosphates and triphosphates of the same nucleoside (ADP and ATP). These observations are demonstrated in correlation plots for selected nucleotide pairs (see Figure S11). This is surprising because these species participate in many of the same reactions, and therefore they exhibit low pathway distances. A possible explanation for the correlations between mono-, di-, and triphosphates of different nucleosides is their link to the energy state of the cell. High ATP levels are indicative of high energy that might promote the formation GTP, UTP, and CTP, which are also molecules with high energy content.

## CONCLUSIONS

The combination of fluorescence microscopy with single-cell analysis by capillary microsampling MS enables selective molecular analysis of an identified subpopulation with specific biological properties and/or functions. This method has the potential for broad applications in untargeted metabolic analysis of cellular subtypes in isogenic populations, such as analysis of stem cells.[49] The specific example described in this paper explores the metabolic differences between four mitotic stages and cytokinesis during cell division. Unlike conventional studies of cell division based on large cell populations, single-cell analysis of selected subpopulations reveals the differences between them and the cellular heterogeneity within them. Significant differences found in cellular energy indicate that metaphase is a high-energy state compared to the other mitotic stages. The ratiometric indicator [GTP]/[GDP] is highest in cytokinesis, which is consistent with increased polymerization of microtubules in this stage. Many of the metabolite abundances exhibited non-normal distributions with long tails showing an increased level of metabolic noise, indicating a higher degree of fluctuations for relative metabolite levels among individual cells. Correlations between the noise levels of transcripts, proteins, and metabolites and their dependence on copy numbers can lead to a deeper understanding of synthetic processes. Our findings illustrate the usefulness of subpopulation analysis based on fluorescent microscopy and single-cell MS. Applications of the combination of the two methods can provide new insight into cell differentiation, disease development, and other areas of biomedicine.

## ASSOCIATED CONTENT

### Supporting Information

The Supporting Information is available free of charge on the ACS Publications website at DOI: 10.1021/acs.analchem.7b05126.

Additional text describing prometaphase arrest by nocodazole and in-source fragmentation induced by ESI; 11 figures showing mitotic arrest by nocodazole, microscope image of a capillary tip with cell contents, fluorescence microscopic images and mass spectra of cells in different mitotic stages, examples of tandem mass spectra used for metabolite assignments, in-source fragmentation induced by ESI, OPLS-DA plot for cells in prometaphase and metaphase, normalized metabolite ion intensities, metabolites with statistically significant regulation between specific mitotic stages, Pearson correlation analysis of intensities of 40 ion species, and scatter matrix for nucleotide−nucleotide correlations;

five tables listing metabolite and lipid species assignments from single mitotic HepG2/C3A cells, various descriptive statistics, and metabolite pairs with statistically significant correlations (PDF)

## AUTHOR INFORMATION

### Corresponding Author
*E-mail vertes@gwu.edu; phone +1 (202) 994-2717; fax +1 (202) 994-5873.

### ORCID
Akos Vertes: 0000-0001-5186-5352

### Notes
The authors declare no competing financial interest.

## REFERENCES

(1) Song, J. L.; Chen, C.; Yuan, J. P.; Sun, S. R. Cancer Med. 2016, 5, 3475−3488.
(2) Sivakumar, S.; Daum, J. R.; Gorbsky, G. J. In Methods Mol. Biol., 2nd ed.; Noguchi, E., Gadaleta, M. C., Eds.; Methods in Molecular Biology (Methods and Protocols), Vol.1170; Humana Press: New York, 2014; pp 549−562; DOI: 10.1007/978-1-4939-0888-2_31.
(3) Jouin, H.; Daher, W.; Khalife, J.; Ricard, I.; Puijalon, O. M.; Capron, M.; Dive, D. Cytometry 2004, 57A, 34−38.
(4) Greve, B.; Kelsch, R.; Spaniol, K.; Eich, H. T.; Gotte, M. Cytometry, Part A 2012, 81A, 284−293.
(5) Bendall, S. C.; Simonds, E. F.; Qiu, P.; Amir, E. A. D.; Krutzik, P. O.; Finck, R.; Bruggner, R. V.; Melamed, R.; Trejo, A.; Ornatsky, O. I.; Balderas, R. S.; Plevritis, S. K.; Sachs, K.; Pe'er, D.; Tanner, S. D.; Nolan, G. P. Science 2011, 332, 687−696.
(6) Borri, A.; Palumbo, P.; Singh, A. IET Syst. Biol. 2016, 10, 179−186.
(7) Oyarzun, D. A.; Lugagne, J. B.; Stan, G. B. V. ACS Synth. Biol. 2015, 4, 116−125.
(8) Rubakhin, S. S.; Romanova, E. V.; Nemes, P.; Sweedler, J. V. Nat. Methods 2011, 8, S20−S29.
(9) Zenobi, R. Science 2013, 342, 1243259.
(10) Zhang, L.; Vertes, A. Anal. Chem. 2015, 87, 10397−10405.
(11) Chen, X.; Love, J. C.; Navin, N. E.; Pachter, L.; Stubbington, M. J. T.; Svensson, V.; Sweedler, J. V.; Teichmann, S. A. Nat. Biotechnol. 2016, 34, 1111−1118.
(12) Passarelli, M. K.; Newman, C. F.; Marshall, P. S.; West, A.; Gilmore, I. S.; Bunch, J.; Alexander, M. R.; Dollery, C. T. Anal. Chem. 2015, 87, 6696−6702.
(13) Ibanez, A. J.; Fagerer, S. R.; Schmidt, A. M.; Urban, P. L.; Jefimovs, K.; Geiger, P.; Dechant, R.; Heinemann, M.; Zenobi, R. Proc. Natl. Acad. Sci. U. S. A. 2013, 110, 8790−8794.
(14) Ong, T. H.; Kissick, D. J.; Jansson, E. T.; Comi, T. J.; Romanova, E. V.; Rubakhin, S. S.; Sweedler, J. V. Anal. Chem. 2015, 87, 7036−7042.
(15) Comi, T. J.; Makurath, M. A.; Philip, M. C.; Rubakhin, S. S.; Sweedler, J. V. Anal. Chem. 2017, 89, 7765−7772.
(16) Shrestha, B.; Vertes, A. Anal. Chem. 2009, 81, 8265−8271.

(17) Stolee, J. A.; Shrestha, B.; Mengistu, G.; Vertes, A. *Angew. Chem., Int. Ed.* **2012**, *51*, 10386−10389.

(18) Fujii, T.; Matsuda, S.; Tejedor, M. L.; Esaki, T.; Sakane, I.; Mizuno, H.; Tsuyama, N.; Masujima, T. *Nat. Protoc.* **2015**, *10*, 1445−1456.

(19) Esaki, T.; Masujima, T. *Anal. Sci.* **2015**, *31*, 1211−1213.

(20) Pan, N.; Rao, W.; Kothapalli, N. R.; Liu, R. M.; Burgett, A. W. G.; Yang, Z. B. *Anal. Chem.* **2014**, *86*, 9376−9380.

(21) Zhang, L.; Foreman, D. P.; Grant, P. A.; Shrestha, B.; Moody, S. A.; Villiers, F.; Kwak, J. M.; Vertes, A. *Analyst* **2014**, *139*, 5079−5085.

(22) Haraguchi, T.; Kaneda, T.; Hiraoka, Y. *Genes Cells* **1997**, *2*, 369−380.

(23) Hesse, M.; Raulf, A.; Pilz, G. A.; Haberlandt, C.; Klein, A. M.; Jabs, R.; Zaehres, H.; Fugemann, C. J.; Zimmermann, K.; Trebicka, J.; Welz, A.; Pfeifer, A.; Roll, W.; Kotlikoff, M. I.; Steinhauser, C.; Gotz, M.; Scholer, H. R.; Fleischmann, B. K. *Nat. Commun.* **2012**, *3*, No. 1076.

(24) Feng, R. Z.; Xu, Y. Q.; Zhao, H. W.; Duan, X. M.; Sun, S. G. *Analyst* **2016**, *141*, 3219−3223.

(25) Roccio, M.; Schmitter, D.; Knobloch, M.; Okawa, Y.; Sage, D.; Lutolf, M. P. *Development* **2013**, *140*, 459−470.

(26) Li, H. D.; Babiarz, J.; Woodbury, J.; Kane-Goldsmith, N.; Grumet, M. *Dev. Biol.* **2004**, *271*, 225−238.

(27) Shah, A. T.; Diggins, K. E.; Walsh, A. J.; Irish, J. M.; Skala, M. C. *Neoplasia* **2015**, *17*, 862−870.

(28) Otsu, N. *IEEE Trans. Syst. Man Cybern. B Cybern.* **1979**, *9*, 62−66.

(29) Schneider, C. A.; Rasband, W. S.; Eliceiri, K. W. *Nat. Methods* **2012**, *9*, 671−675.

(30) Strohalm, M.; Hassman, M.; Kosata, B.; Kodicek, M. *Rapid Commun. Mass Spectrom.* **2008**, *22*, 905−908.

(31) Xia, J. G.; Sinelnikov, I. V.; Han, B.; Wishart, D. S. *Nucleic Acids Res.* **2015**, *43*, W251−W257.

(32) Paglia, G.; Williams, J. P.; Menikarachchi, L.; Thompson, J. W.; Tyldesley-Worster, R.; Halldorsson, S.; Rolfsson, O.; Moseley, A.; Grant, D.; Langridge, J.; Palsson, B. O.; Astarita, G. *Anal. Chem.* **2014**, *86*, 3985−3993.

(33) Paglia, G.; Kliman, M.; Claude, E.; Geromanos, S.; Astarita, G. *Anal. Bioanal. Chem.* **2015**, *407*, 4995−5007.

(34) Xu, Y. F.; Lu, W. Y.; Rabinowitz, J. D. *Anal. Chem.* **2015**, *87*, 2273−2281.

(35) Yang, M. S.; Yu, L. C.; Gupta, R. C. *Toxicology* **2004**, *201*, 105−113.

(36) Fong, J. J.; Nguyen, B. L.; Bridger, R.; Medrano, E. E.; Wells, L.; Pan, S. J.; Sifers, R. N. *J. Biol. Chem.* **2012**, *287*, 12195−12203.

(37) Slawson, C.; Copeland, R. J.; Hart, G. W. *Trends Biochem. Sci.* **2010**, *35*, 547−555.

(38) Hardie, D. G. *Genes Dev.* **2011**, *25*, 1895−1908.

(39) Jeon, S.-M. *Exp. Mol. Med.* **2016**, *48*, e245.

(40) Hardie, D. G.; Ross, F. A.; Hawley, S. A. *Nat. Rev. Mol. Cell Biol.* **2012**, *13*, 251−262.

(41) Miniowitz-Shemtov, S.; Teichner, A.; Sitry-Shevah, D.; Hershko, A. *Proc. Natl. Acad. Sci. U. S. A.* **2010**, *107*, 5351−5356.

(42) Teichner, A.; Eytan, E.; Sitry-Shevah, D.; Miniowitz-Shemtov, S.; Dumin, E.; Gromis, J.; Hershko, A. *Proc. Natl. Acad. Sci. U. S. A.* **2011**, *108*, 3187−3192.

(43) Akhmanova, A.; Steinmetz, M. O. *Nat. Rev. Mol. Cell Biol.* **2015**, *16*, 711−726.

(44) Park, J. O.; Rubin, S. A.; Xu, Y. F.; Amador-Noguez, D.; Fan, J.; Shlomi, T.; Rabinowitz, J. D. *Nat. Chem. Biol.* **2016**, *12*, 482−489.

(45) Arkin, A.; Shen, P.; Ross, J. *Science* **1997**, *277*, 1275−1279.

(46) Kharchenko, P.; Church, G. M.; Vitkup, D. *Mol. Syst. Biol.* **2005**, *1* (2005), No. 0016.

(47) Walther, D.; Strassburg, K.; Durek, P.; Kopka, J. *OMICS* **2010**, *14*, 261−274.

(48) Redestig, H.; Costa, I. G. *Bioinformatics* **2011**, *27*, i357−i365.

(49) Quinn, K. P.; Sridharan, G. V.; Hayden, R. S.; Kaplan, D. L.; Lee, K.; Georgakoudi, I. *Sci. Rep.* **2013**, *3*, No. 3432.

Supporting Information for

# Single-Cell Mass Spectrometry of Subpopulations Selected by Fluorescence Microscopy

Linwen Zhang,[†] Christopher J. Sevinsky,[‡] Brian M. Davis,[‡] and Akos Vertes*,[†]

[†]Department of Chemistry, The George Washington University, Washington, District of Columbia 20052, United States

[‡]GE Global Research, Niskayuna, New York 12309, United States

*To whom correspondence should be addressed. E-mail: vertes@gwu.edu; phone: +1 (202) 994-2717; fax: +1 (202) 994-5873.

# Table of Contents

**Prometaphase Arrest by Nocodazole.** Nocodazole is widely used for the synchronization of cell populations by reversibly arresting the cell cycle at the G2/M phase.[1] It is thought to act through preventing the GTP mediated polymerization of tubulin dimers into microtubules,[2] and shifting the microtubule dynamics toward the depolymerized form.[3-4] To confirm the effect of mitotic arrest on cell populations induced by nocodazole, flow cytometry, confocal microscopy, and immunocytochemistry were performed. Figure S1a shows the distributions of DNA content in untreated, vehicle (DMSO) treated, and nocodazole treated cells by flow cytometry using propidium iodide (PI) staining. In the nocodazole treated cells, 89% of the cells accumulate in G2/M phase compared to 28% in the untreated and 33% in the vehicle treated cells. This result indicates that 24 h nocodazole treatment can effectively arrest the cell cycle in the G2/M phase.

More accurate identification of the arrest position was found by confocal imaging of cells with the nuclear DNA stained by DAPI (dark blue), the α-tubulin labeled by mouse monoclonal antibody against α-tubulin (red), and the histone H3 stained by rabbit polyclonal antibody against phospho-histone H3 (light blue). The latter is indicative of the phosphorylation of Ser10 in histone H3 that has been correlated with chromatin condensation is abundant in prometaphase.[5] Figure S1b shows the images of HepG2/C3A cells treated for 24 h with vehicle (0.1% DMSO) and 100 ng/ml nocodazole, respectively. Compared with the vehicle control, more of the nocodazole treated cells are in prometaphase indicated by the condensed chromosomes stained in light blue. This observation points to cell cycle arrest in prometaphase.

Significantly increased α-tubulin and β-tubulin levels were also observed ($p < 0.0001$ in both cases based on two-tailed $t$ tests) in nocodazole treated cells by immunocytochemistry and quantitative image segmentation (see Figure S1c). The elevated tubulin levels are likely due to the lack of assembly of heterodimers into microtubules blocked by nocodazole treatment. This

effect may be due to a compensatory cellular mechanism to drive microtubule polymerization by increasing tubulin content.

**In-Source Fragmentation Induced by ESI.** Due to in-source fragmentation of some metabolite ions produced by ESI, corrections need to be applied for the measured metabolite abundances.[6] Mass spectra for chemical standard solutions with their concentrations similar to mammalian intracellular metabolite levels were measured by ESI-IMS-MS.[7] For example, the ESI-IMS mass spectra of 10.0 mM glutamine, 10.0 mM glutamate, 1.0 mM glucose 6-phosphate (G-6-P), 1.0 mM fructose 1,6-bisphosphate (F-1,6-bis-P), 1.0 mM GSH, 0.05 mM AMP, 0.5 mM ADP, 5.0 mM ATP, 0.01 mM GDP, 1.0 mM GTP, 0.1 mM GDP-fucose, 1.0 mM UDP-glucose, and 1.0 mM UDP-N-acetylglucosamine (UDP-GlcNAc) are shown in Figure S2. Formation of quasi-molecular ions and their fragments can be observed in these spectra. Corrections to the molecular ion intensities are based on the observed survival yields. Some of the metabolite ions, such as the molecular ions of ADP, AMP, and GDP, not only decay to produce their fragment ions, but they themselves are formed as fragments of larger ions. For example, in the spectrum of GDP standard, 64% is the survival yield for the GDP molecular ion. Also, GDP molecular ions are detected as fragments in GTP and GDP-fucose spectra with 36% and 10% relative abundances, respectively. This means that in a complex mixture containing GDP, GTP, and GDP-fucose the following correction can be made: $[GDP]_{corr} = ([GDP]_{meas}-[GTP]_{corr}\times0.36-[GDP\text{-}fucose]_{corr}\times0.1)/0.64$, where the "corr" and "meas" subscripts stand for the corrected and measured values, respectively. Potential interferences for metabolites with structural isomers also have to be considered.[6] The tandem mass spectra of the ions with *m/z* 346.053, 426.021 and 505.985 from the cell lysates are consistent with AMP, ADP, and ATP, respectively, but not with the structural isomers, dGMP, dGDP, and dGTP. However, for the ion with *m/z* 130.085 the annotation can be leucine and

isoleucine, and the *m/z* 259.021 peak is consistent with glucose-6-phosphate, fructose-6-phosphate, and fructose-1-phosphate. Thus, these species cannot be differentiated based on *m/z* values alone.

**SUPPORTING FIGURES**

**(a)**



**(b)**



**(c)**
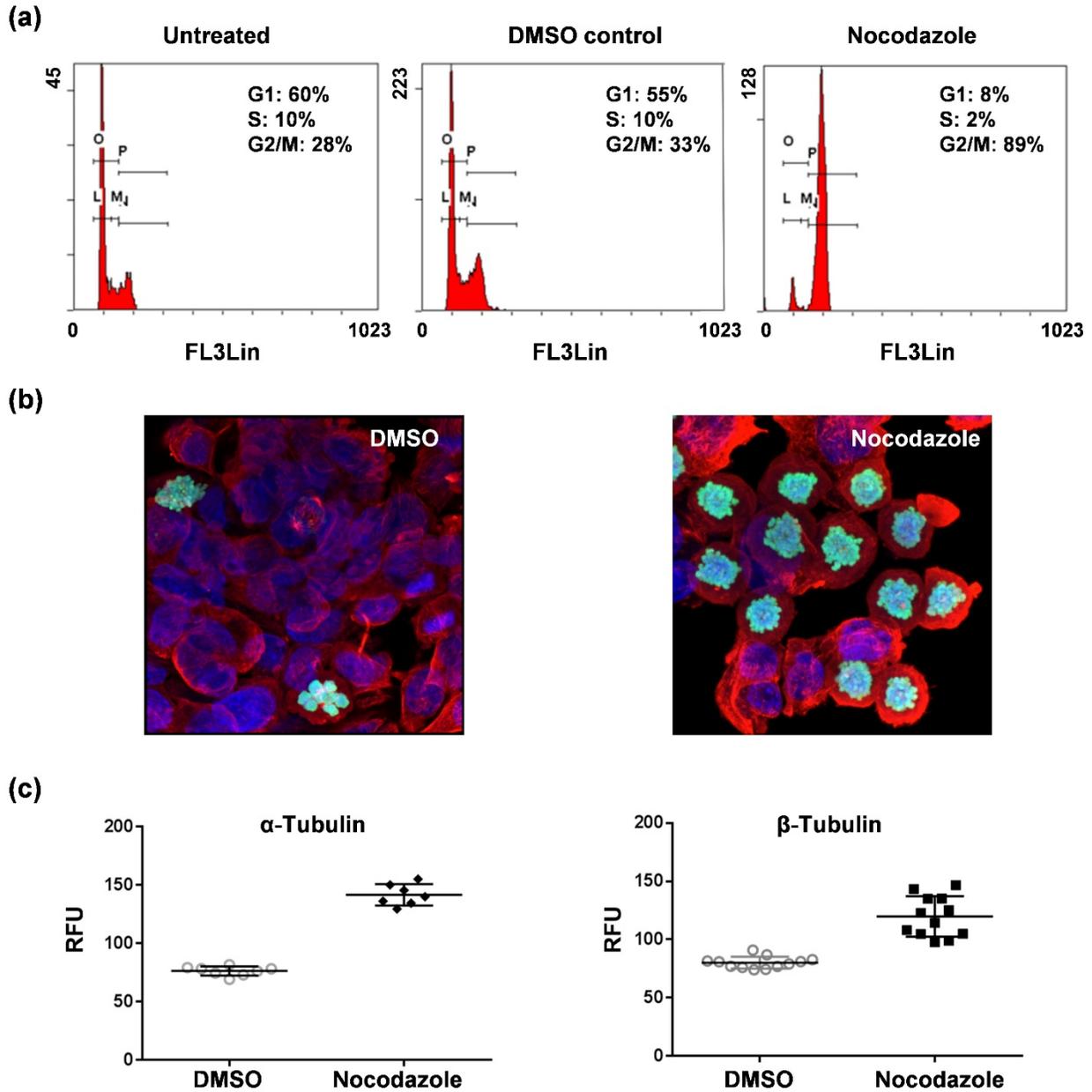


**Figure S1.** (a) Flow cytometry indicates that nocodazole treatment results in a cell population enriched in G2/M state (89%) compared to vehicle (DMSO) treated (33%) and untreated (28%) cells. (b) Confocal microscopy images of hepatocytes treated by vehicle alone (left) and nocodazole (right). Cells are stained for DNA (dark blue), α-tubulin (red) and histone H3 (light blue). (c) Increased levels of α-tubulin and β-tubulin (in relative fluorescence units) are indicated by immunocytochemistry for nocodazole treated cells compared to vehicle.
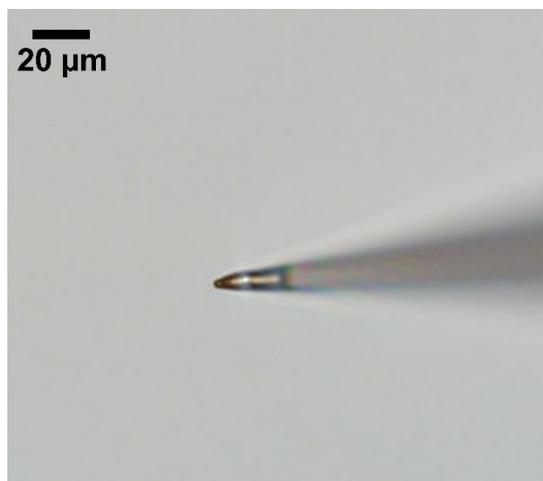
**Figure S2.** Microscopic image of a capillary tip with cell contents. The volume of extracted cell contents was estimated to be ~0.2 pL.
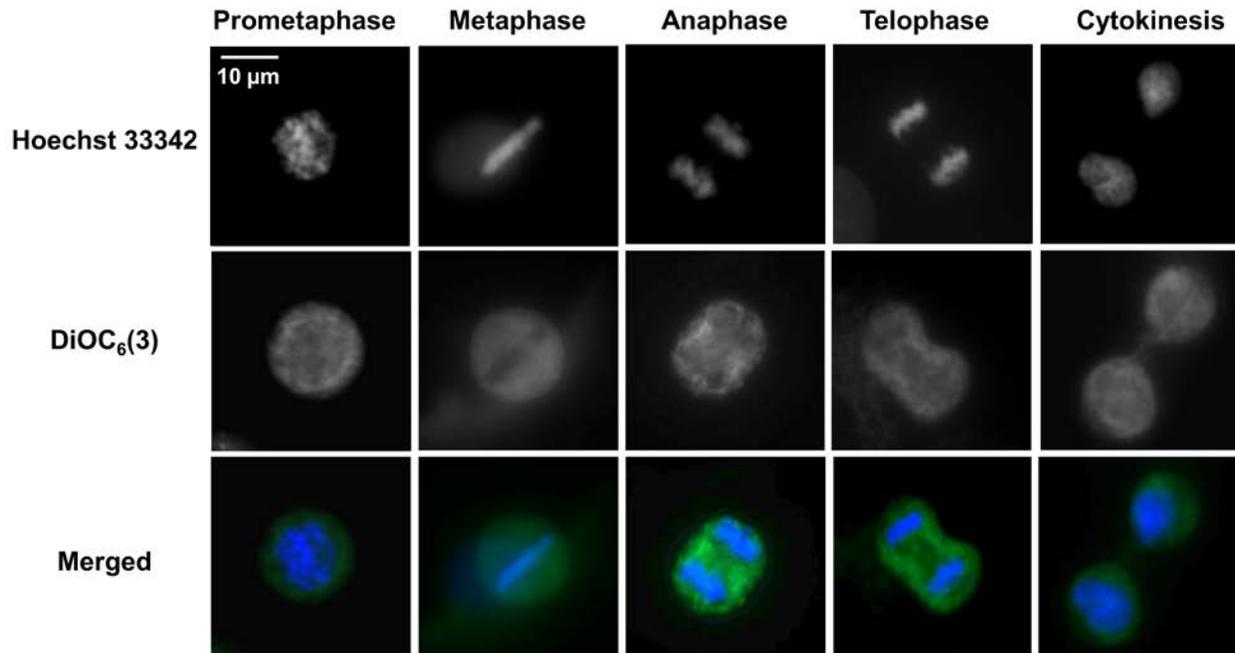
**Figure S3.** Fluorescence microscopic images of cells at distinct mitotic stages shown (top row) with the double stranded DNA stained by Hoechst 33342, (middle row) endoplasmic reticulum stained by $DiOC_6(3)$, and (bottom row) the corresponding merged images. In prometaphase, the nuclear envelop breaks and condensed chromosomes are observed. In metaphase, chromosomes are lined up along the cell equator. The separation of two pairs of chromatids towards the opposite poles of the cells are observed in anaphase followed by the formation of a cleavage furrow in telophase. During cytokinesis, the cytoplasm separates into two parts and two new cells are formed.
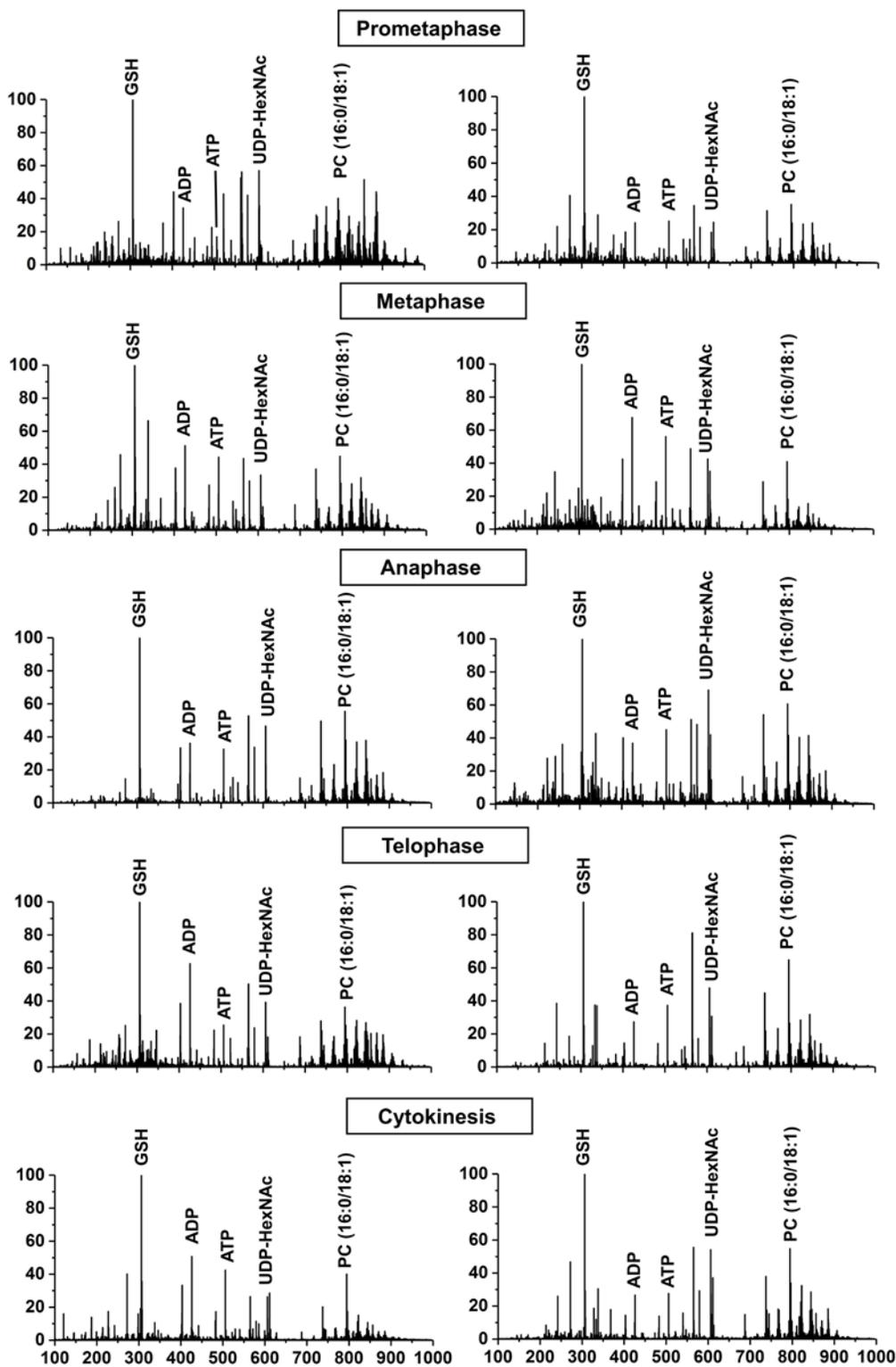
**Figure S4.** Single-cell mass spectra obtained from cells in different mitotic stages. Some of the assigned metabolites and lipids are labeled.
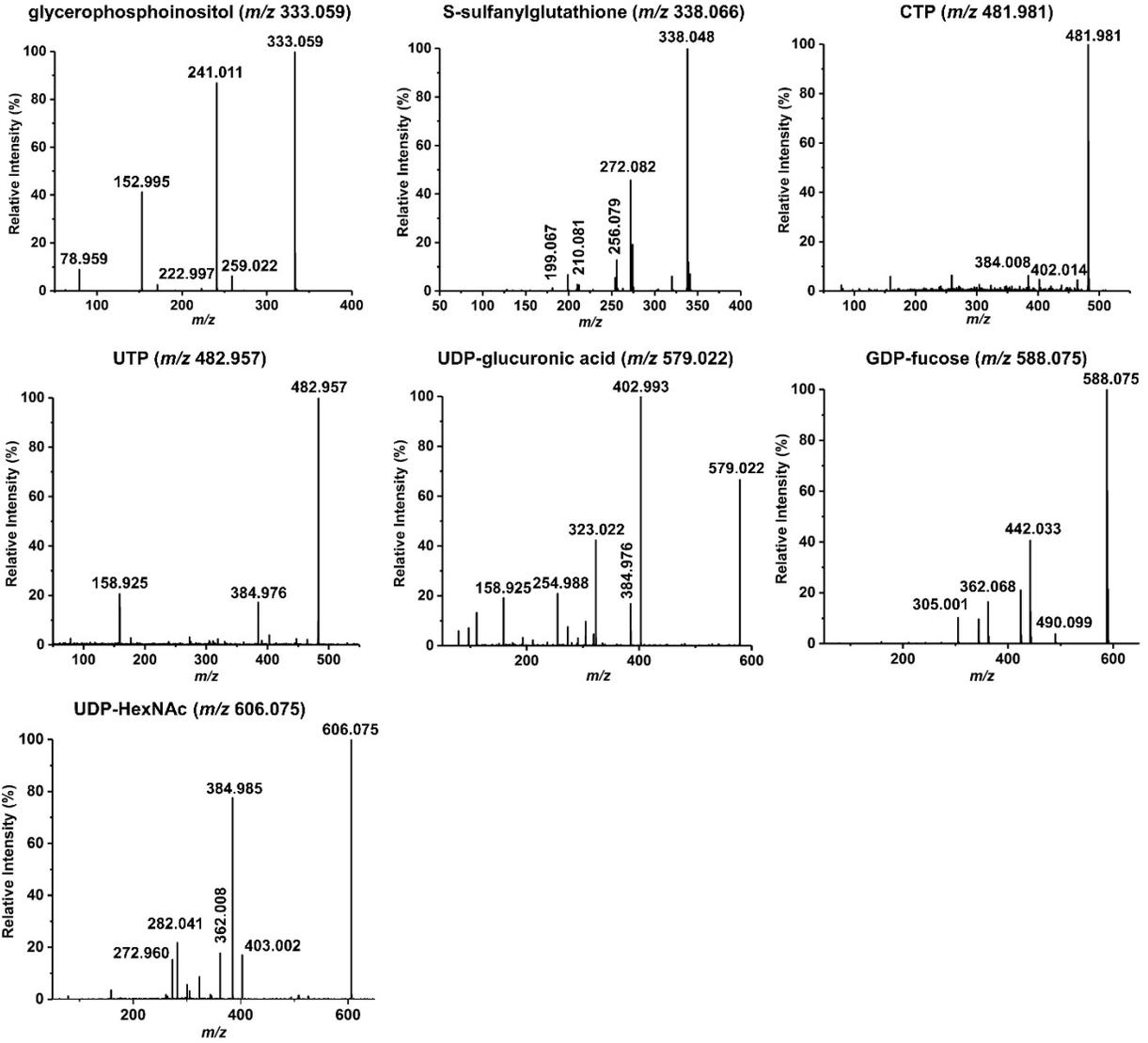
**Figure S5.** Tandem mass spectra obtained from cell lysates for metabolite assignments.

**(m)**
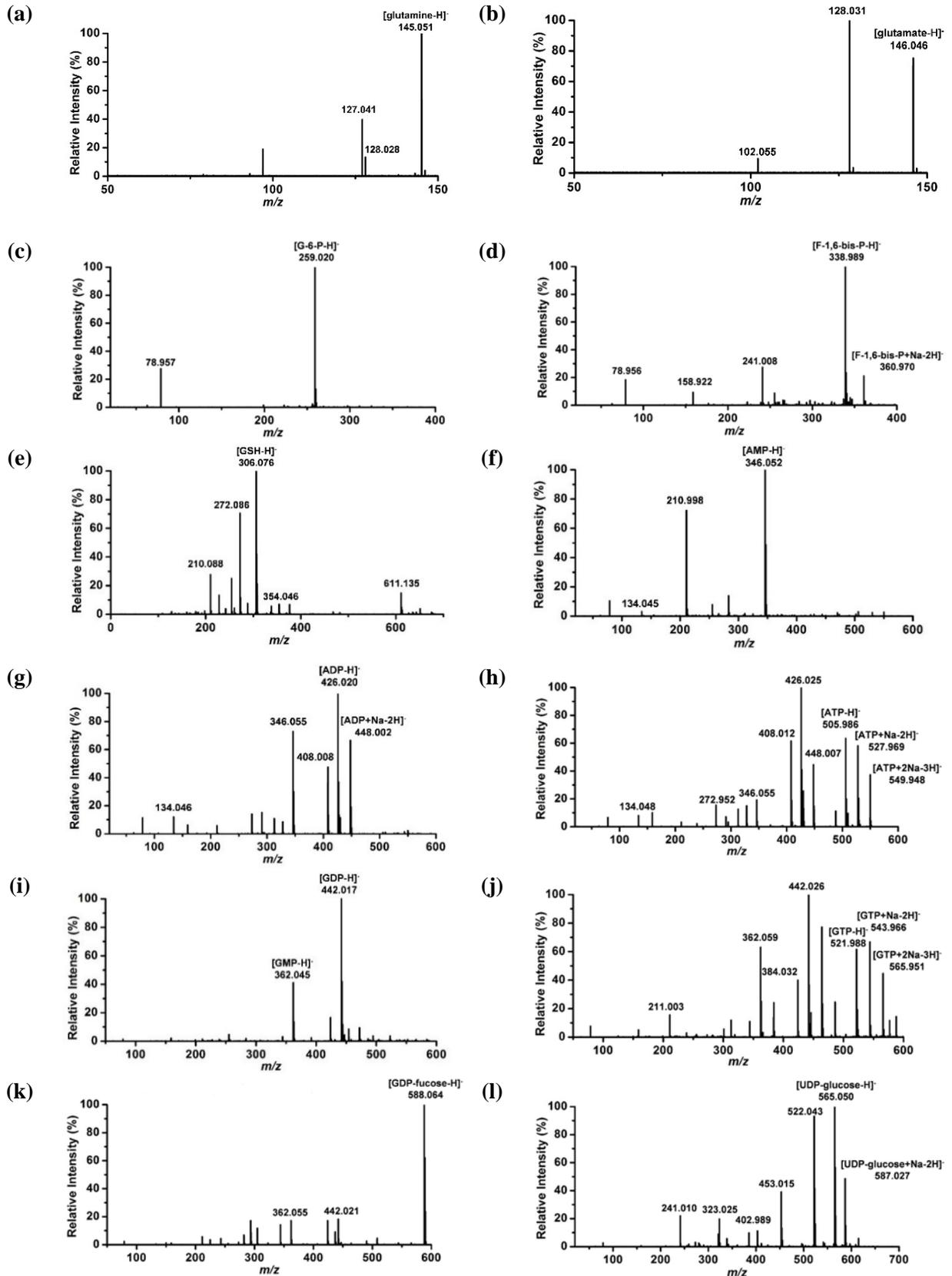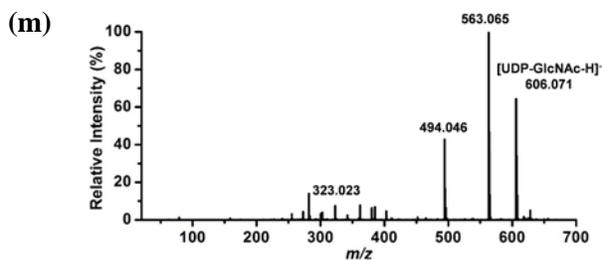


**Figure S6.** Mass spectra of (**a**) 10.0 mM glutamine, (**b**) 10.0 mM glutamate, (**c**) 1.0 mM glucose 6-phosphate (G-6-P), (**d**) 1.0 mM fructose 1,6-bisphosphate (F-1,6-bis-P), (**e**) 1.0 mM GSH, (**f**) 0.05 mM AMP, (**g**) 0.5 mM ADP, (**h**) 5.0 mM ATP, (**i**) 0.01 mM GDP, (**j**) 1.0 mM GTP, (**k**) 0.1 mM GDP-fucose, (**l**) 1.0 mM UDP-glucose, and (**m**) 1.0 mM UDP-GlcNAc standard solutions produced by ESI-IMS-MS show in-source fragmentation for these metabolites.
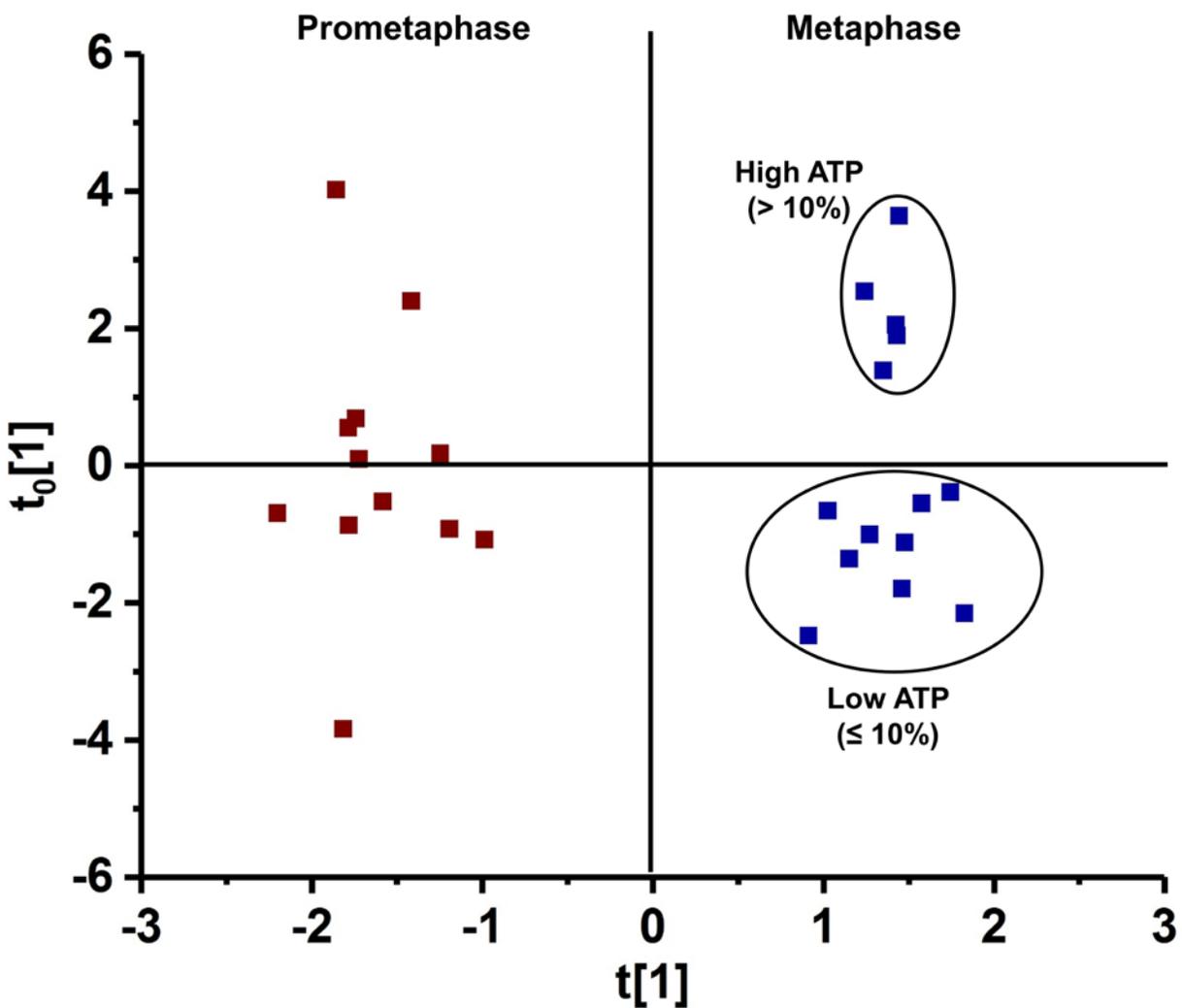
**Figure S7.** OPLS-DA scatter plot for comparison of the single-cell mass spectra obtained from cells in prometaphase and metaphase. Subpopulations with high (> 10%) and low ATP levels (≤ 10%) in cells are distinguished in metaphase.
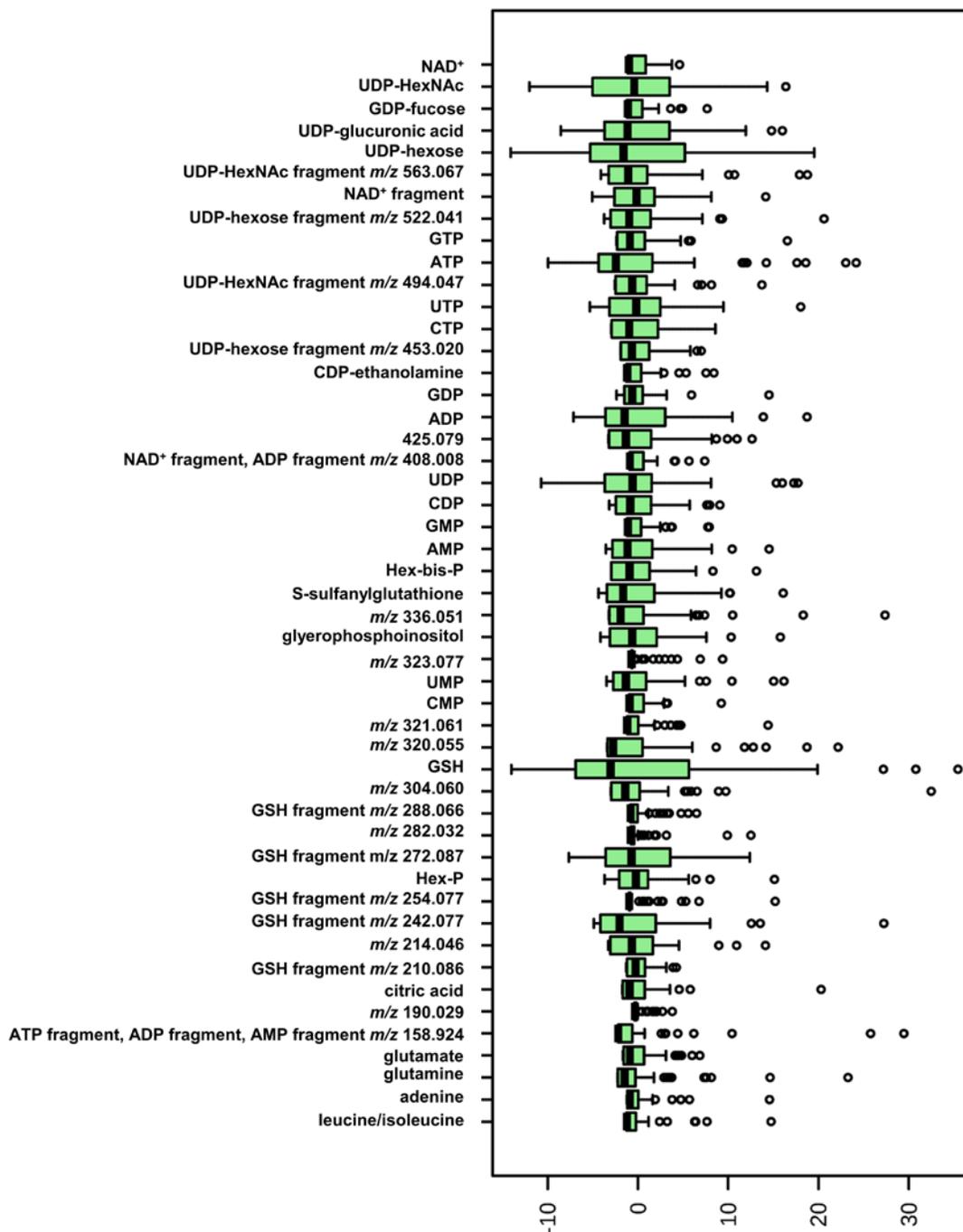
**Figure S8.** Ion abundances from overall mitotic cell population (n = 59) are normalized by sum of cell-related peak intensities followed by Pareto scaling.
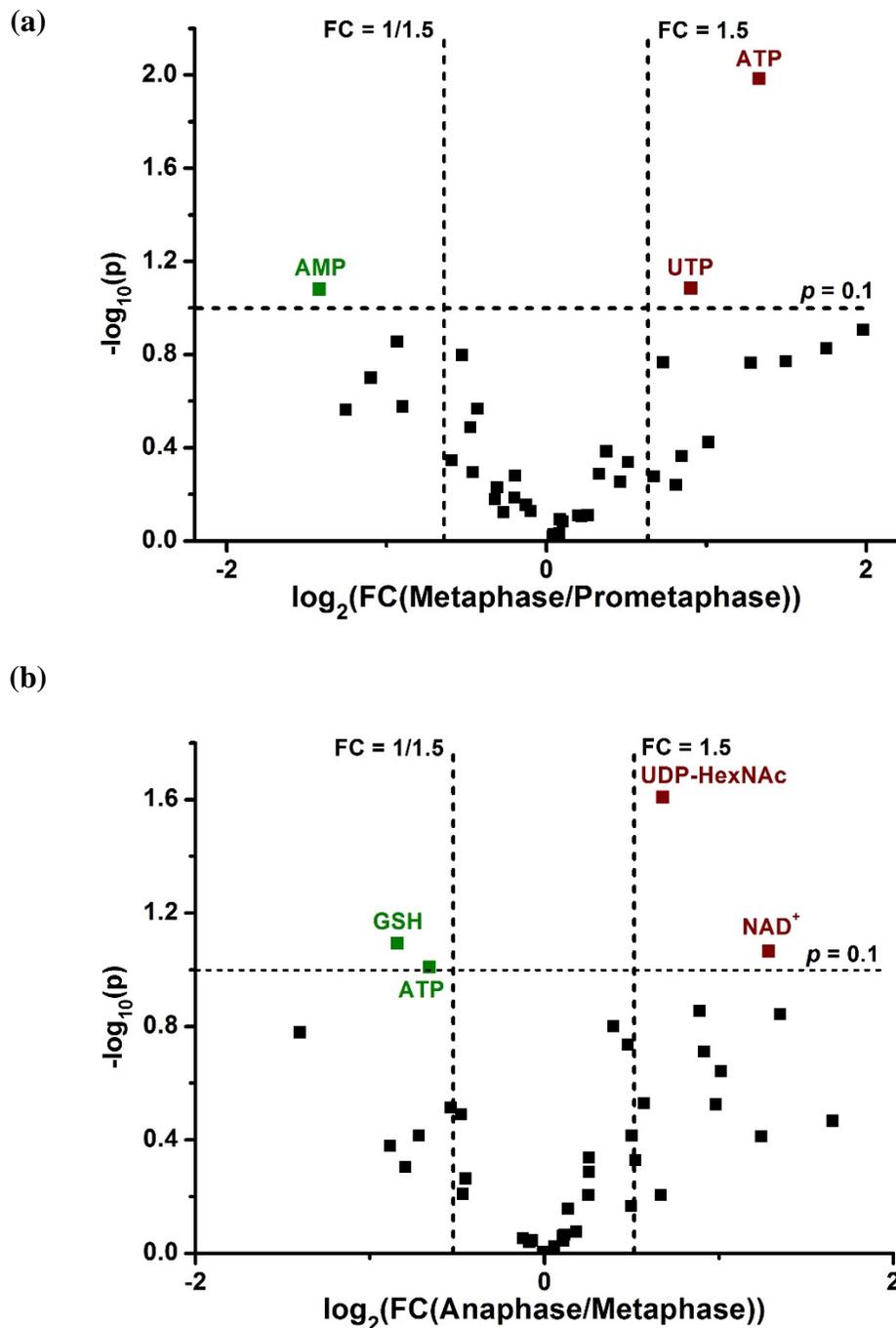
**Figure S9.** Volcano plots visualize metabolites with statistically significant fold changes between (**a**) prometaphase and metaphase, and (**b**) metaphase and anaphase. Metabolites that show down- (green) or up-regulation (red) are selected based on fold change (FC) cutoff values of FC $\leq$ 1/1.5 or FC $\geq$ 1.5, respectively, and a statistical significance of $p < 0.1$.
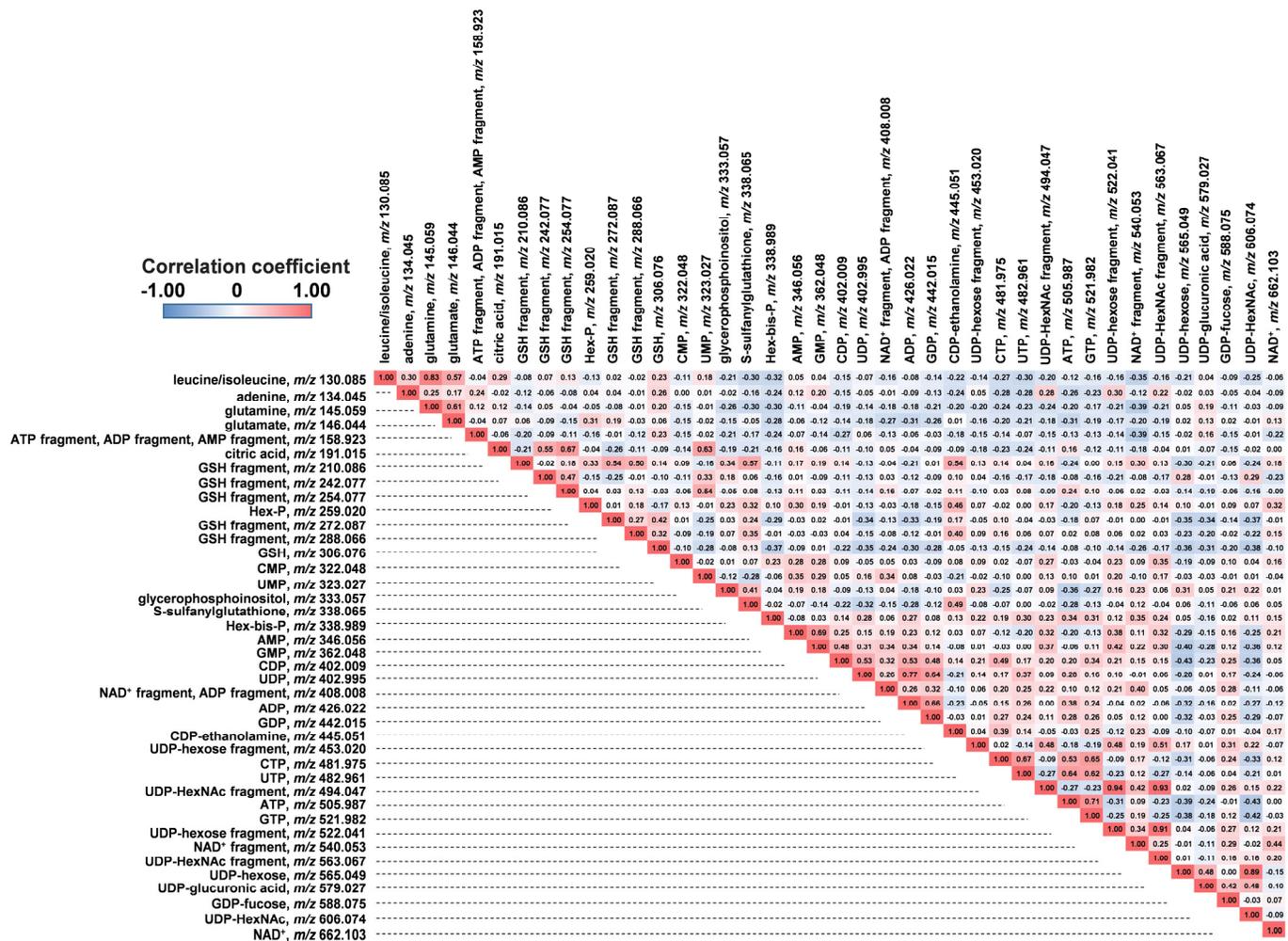
**Figure S10.** Pearson correlation analysis of ion intensities for 40 deisotoped peaks from 59 mass spectra corresponding to individual mitotic cells. For visualization, cells with the correlation coefficient values are colored on a graded scale from -1.00 corresponding to darkest blue, 0.00 representing midpoint with white, and +1.00 corresponding to darkest red.
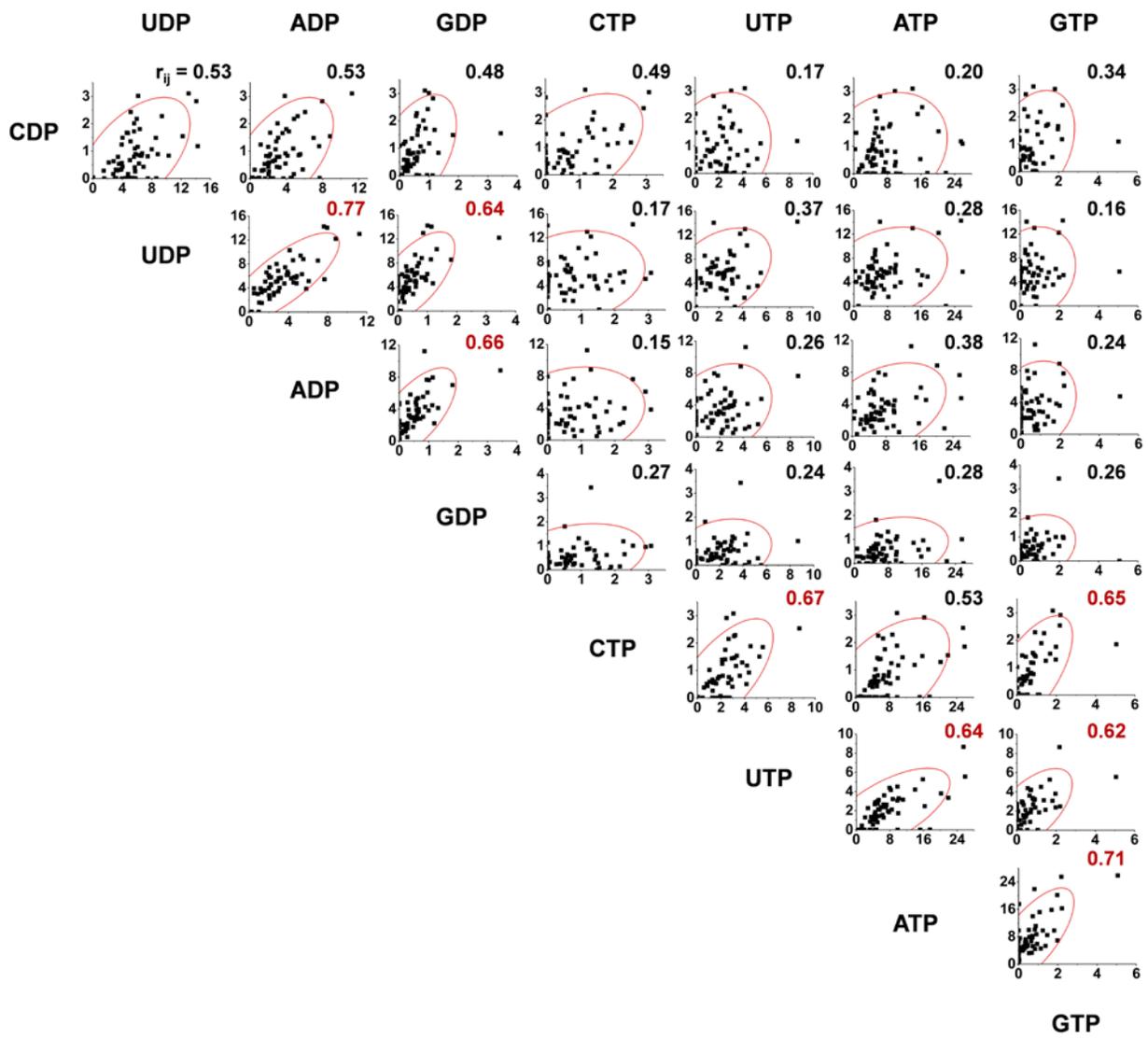
**Figure S11.** Correlation of normalized ion intensities for selected nucleotides for 59 cells, corresponding correlation coefficients, $r_{ij}$, ($r_{ij} > 0.55$ in red, and $r_{ij} \leq 0.55$ in black), and 95% confidence ellipse.

## SUPPORTING TABLES

**Table S1.** Metabolite assignments from single mitotic HepG2/C3A cells based on accurate mass measurements, CCS determination and tandem MS.

| Name | Formula | $m_{meas}$ (Da) | $m_{calc}$ (Da) | $\Delta m$ (mDa) | $CCS_{meas}$ ($\mathring{A}^2$) | $CCS_{ref}$ ($\mathring{A}^2$) | $\Delta CCS$ ($\mathring{A}^2$) |
|---|---|---|---|---|---|---|---|
| leucine/isoleucine | $[C_6H_{13}NO_2\text{-}H]^-$ | 130.085 | 130.087 | -2 | 127 | 129[a] | -2 |
| adenine | $[C_5H_5N_5\text{-}H]^-$ | 134.041 | 134.047 | -6 | 114 | 119[a] | -5 |
| glutamine | $[C_5H_{10}N_2O_3\text{-}H]^-$ | 145.056 | 145.062 | -6 | 121 | 126[a] | -5 |
| glutamate | $[C_5H_9NO_4\text{-}H]^-$ | 146.040 | 146.046 | -6 | 119 | 123[a] | -4 |
| citric acid | $[C_6H_8O_7\text{-}H]^-$ | 191.018 | 191.019 | -1 | 125 | 127[a] | -2 |
| Hex-P | $[C_6H_{13}O_9P\text{-}H]^-$ | 259.020 | 259.022 | -2 | 143 | 143[a] | 0 |
| GSH | $[C_{10}H_{17}N_3O_6S\text{-}H]^-$ | 306.076 | 306.076 | 0 | 158 | 159[a] | -1 |
| | $[C_{10}H_{16}N_3O_6S+Na\text{-}2H]^-$ | 328.057 | 328.058 | -1 | 160 | 160[a] | 0 |
| CMP | $[C_9H_{14}N_3O_8P\text{-}H]^-$ | 322.042 | 322.045 | -3 | 159 | 160[a] | -1 |
| UMP | $[C_9H_{13}N_2O_9P\text{-}H]^-$ | 323.027 | 323.029 | -2 | 157 | 158[a] | -1 |
| glycerophosphoinositol | $[C_9H_{19}O_{11}P\text{-}H]^-$ | 333.069 | 333.059 | 10 | 161 | | |
| S-sulfanylglutathione | $[C_{10}H_{17}N_3O_6S\text{-}H]^-$ | 338.066 | 338.048 | 18 | 164 | | |
| Hex-bis-P | $[C_6H_{14}O_{12}P_2\text{-}H]^-$ | 338.984 | 338.989 | -5 | 152 | 150[a] | 2 |
| AMP | $[C_{10}H_{15}N_5O_7P\text{-}H]^-$ | 346.053 | 346.056 | -3 | 168 | 169[a] | -1 |
| GMP | $[C_{10}H_{14}N_5O_8P\text{-}H]^-$ | 362.045 | 362.051 | -6 | 163 | 165[a] | -2 |
| CDP | $[C_9H_{15}N_3O_{11}P_2\text{-}H]^-$ | 402.008 | 402.011 | -3 | 172 | 170[a] | -2 |
| UDP | $[C_9H_{14}N_2O_{12}P_2\text{-}H]^-$ | 402.994 | 402.995 | -1 | 168 | 169[a] | -1 |
| ADP | $[C_{10}H_{15}N_5O_{10}P_2\text{-}H]^-$ | 426.021 | 426.022 | -1 | 181 | 180[a] | 1 |
| | $[C_{10}H_{15}N_5O_{10}P_2+Na\text{-}2H]^-$ | 448.003 | 448.004 | -1 | 185 | 184.2[b] | 1 |
| GDP | $[C_{10}H_{15}N_5O_{11}P_2\text{-}H]^-$ | 442.014 | 442.017 | -3 | 177 | 178[a] | -1 |
| CDP-ethanolamine | $[C_{11}H_{20}N_4O_{11}P_2\text{-}H]^-$ | 445.052 | 445.053 | -1 | 185 | | |
| CTP | $[C_9H_{16}N_3O_{14}P_3\text{-}H]^-$ | 481.975 | 481.977 | -2 | 179 | | |
| UTP | $[C_9H_{15}N_2O_{15}P_3\text{-}H]^-$ | 482.953 | 482.961 | -8 | 178 | | |

| | | | | | | | |
|---|---|---|---|---|---|---|---|
| ATP | [C$_{10}$H$_{16}$N$_5$O$_{13}$P$_3$-H]$^-$ | 505.985 | 505.989 | -4 | 189 | 192$^b$ | -3 |
| | [C$_{10}$H$_{16}$N$_5$O$_{13}$P$_3$+Na-2H]$^-$ | 527.964 | 527.970 | -6 | 193 | 194$^b$ | -1 |
| | [C$_{10}$H$_{16}$N$_5$O$_{13}$P$_3$+K-2H]$^-$ | 543.949 | 543.944 | 5 | 195 | 199$^b$ | -4 |
| GTP | [C$_{10}$H$_{16}$N$_5$O$_{14}$P$_3$-H]$^-$ | 521.977 | 521.983 | -6 | 191 | 190$^a$ | 1 |
| UDP-xylose | [C$_{14}$H$_{22}$N$_2$O$_{16}$P$_2$-H]$^-$ | 535.024 | 535.037 | -13 | 203 | | |
| UDP-hexose | [C$_{15}$H$_{24}$N$_2$O$_{17}$P$_2$-H]$^-$ | 565.050 | 565.048 | 2 | 207 | 204$^a$ | 3 |
| UDP-glucuronic acid | [C$_{15}$H$_{22}$N$_2$O$_{18}$P$_2$-H]$^-$ | 579.019 | 579.027 | -8 | 210 | | |
| GDP-fucose | [C$_{16}$H$_{25}$N$_5$O$_{15}$P$_2$-H]$^-$ | 588.063 | 588.075 | -12 | 211 | | |
| UDP-HexNAc | [C$_{17}$H$_{27}$N$_3$O$_{17}$P$_2$-H]$^-$ | 606.068 | 606.074 | -6 | 222 | | |
| NAD$^+$ | [C$_{21}$H$_{27}$N$_7$O$_{14}$P$_2$-H]$^-$ | 662.095 | 662.102 | -7 | 223 | 226$^a$ | -3 |

[a] CCS values were obtained from the literature.[8]
[b] CCS values were obtained by measuring the corresponding chemical standard.

**Table S2.** Assignments of lipid species from single mitotic HepG2/C3A cells based on accurate mass measurements, CCS determination and tandem MS. The reference CCS values were obtained from the literature.[9]

| Lipid class | Species | Formula | $m_{meas}$ (Da) | $m_{calc}$ (Da) | $\Delta m$ (mDa) | $CCS_{meas}$ ($\text{Å}^2$) | $CCS_{ref}$ ($\text{Å}^2$) | $\Delta CCS$ ($\text{Å}^2$) | Fragments (*m/z*) |
|---|---|---|---|---|---|---|---|---|---|
| SM | d18:1/16:0 | $[C_{39}H_{79}N_2O_6P+Cl]^-$ | 737.535 | 737.537 | -2 | 291 | | | 255, 687 |
| | d18:0/16:0 | $[C_{39}H_{81}N_2O_6P+Cl]^-$ | 739.539 | 739.553 | -14 | 292 | | | 255, 689 |
| PC | 16:1/16:1 | $[C_{40}H_{76}NO_8P+Cl]^-$ | 764.493 | 764.500 | -7 | 292 | | | 253, 714 |
| | 16:0/16:1 | $[C_{40}H_{78}NO_8P+Cl]^-$ | 766.518 | 766.516 | 2 | 294 | | | 253, 255, 716 |
| | 16:0/16:0 | $[C_{40}H_{80}NO_8P+Cl]^-$ | 768.521 | 768.531 | -10 | 295 | | | 255, 718 |
| | 16:1/18:1 | $[C_{42}H_{80}NO_8P+Cl]^-$ | 792.531 | 792.531 | 0 | 299 | | | 253, 281, 742 |
| | 16:0/18:1 | $[C_{42}H_{82}NO_8P+Cl]^-$ | 794.547 | 794.547 | 0 | 301 | | | 255, 281, 744 |
| | 18:1/18:2 | $[C_{44}H_{82}NO_8P+Cl]^-$ | 818.545 | 818.547 | -2 | 304 | | | 279, 281, 768 |
| | 18:1/18:1 | $[C_{44}H_{84}NO_8P+Cl]^-$ | 820.561 | 820.562 | -1 | 305 | | | 281, 770 |
| | 18:0/18:1 | $[C_{44}H_{86}NO_8P+Cl]^-$ | 822.567 | 822.578 | -11 | 307 | | | 281, 283, 772 |
| | 18:1/20:4 | $[C_{46}H_{82}NO_8P+Cl]^-$ | 842.547 | 842.547 | 0 | 307 | | | 281, 303, 792 |
| | 18:1/20:3 | $[C_{46}H_{84}NO_8P+Cl]^-$ | 844.552 | 844.562 | -10 | 309 | | | 281, 305, 794 |
| PA | 16:1/18:1 | $[C_{37}H_{69}O_8P-H]^-$ | 671.467 | 671.466 | 1 | 263 | | | 253, 281, 389, 407, 417, 435 |
| | 16:0/18:1 | $[C_{37}H_{71}O_8P-H]^-$ | 673.485 | 673.481 | 4 | 266 | | | 255, 281, 391, 409, 417, 435 |
| | 18:1/18:1 | $[C_{39}H_{73}O_8P-H]^-$ | 699.499 | 699.497 | 2 | 270 | | | 281, 417, 435 |
| | 18:0/18:1 | $[C_{39}H_{75}O_8P-H]^-$ | 701.513 | 701.513 | 0 | 272 | | | 281, 283, 417, 435, 419, 437 |

| | | | | | | | | |
|---|---|---|---|---|---|---|---|---|
| PE | 16:1/16:1 | [C$_{37}$H$_{70}$NO$_8$P-H]$^-$ | 686.479 | 686.477 | 2 | 263 | | | 253 |
| | 16:0/16:1 | [C$_{37}$H$_{72}$NO$_8$P-H]$^-$ | 688.495 | 688.492 | 3 | 266 | | | 253, 255 |
| | 16:1/18:1 | [C$_{39}$H$_{74}$NO$_8$P-H]$^-$ | 714.509 | 714.508 | 1 | 272 | 271 | 1 | 253, 281 |
| | 16:0/18:1 | [C$_{39}$H$_{76}$NO$_8$P-H]$^-$ | 716.524 | 716.524 | 0 | 274 | 272 | 2 | 255, 281 |
| | 16:0/18:0 | [C$_{39}$H$_{78}$NO$_8$P-H]$^-$ | 718.535 | 718.539 | -4 | 275 | 274 | 1 | 255, 283 |
| | 16:0/20:4 | [C$_{41}$H$_{74}$NO$_8$P-H]$^-$ | 738.508 | 738.508 | 0 | 276 | 274 | 2 | 255, 303 |
| | 18:1/18:2 | [C$_{41}$H$_{76}$NO$_8$P-H]$^-$ | 740.523 | 740.524 | -1 | 277 | 276 | 1 | 279, 281 |
| | 18:1/18:1 | [C$_{41}$H$_{78}$NO$_8$P-H]$^-$ | 742.540 | 742.539 | 1 | 279 | 279 | 0 | 281 |
| | 18:1/18:0 | [C$_{41}$H$_{80}$NO$_8$P-H]$^-$ | 744.554 | 744.555 | -1 | 280 | 281 | -1 | 281, 283 |
| | 16:0/22:6 | [C$_{43}$H$_{74}$NO$_8$P-H]$^-$ | 762.510 | 762.508 | 2 | 281 | 280 | 1 | 255, 327 |
| | 18:1/20:4 | [C$_{43}$H$_{76}$NO$_8$P-H]$^-$ | 764.513 | 764.524 | -11 | 281 | 283 | -2 | 281, 303 |
| | 18:0/20:4 | [C$_{43}$H$_{78}$NO$_8$P-H]$^-$ | 766.538 | 766.539 | -1 | 283 | 284 | -1 | 283, 303 |
| | 18:0/20:3 | [C$_{43}$H$_{80}$NO$_8$P-H]$^-$ | 768.548 | 768.555 | -7 | 284.0 | | | 283, 305 |
| | 18:1/20:1 | [C$_{43}$H$_{82}$NO$_8$P-H]$^-$ | 770.547 | 770.549 | -2 | 285.8 | | | 281, 309 |
| PS | 16:1/16:1 | [C$_{38}$H$_{70}$NO$_{10}$P-H]$^-$ | 730.468 | 730.466 | 2 | 276.7 | | | 253, 643 |
| | 16:0/16:1 | [C$_{38}$H$_{72}$NO$_{10}$P-H]$^-$ | 732.490 | 732.482 | 8 | 278.6 | | | 253, 255, 645 |
| | 16:1/18:1 | [C$_{40}$H$_{74}$NO$_{10}$P-H]$^-$ | 758.505 | 758.498 | 7 | 283 | 280 | 3 | 253, 281, 671 |
| | 16:1/18:0 | [C$_{40}$H$_{76}$NO$_{10}$P-H]$^-$ | 760.514 | 760.513 | 1 | 285 | 282 | 3 | 253, 283, 673 |
| | 18:1/18:2 | [C$_{42}$H$_{76}$NO$_{10}$P-H]$^-$ | 784.516 | 784.513 | 3 | 288 | 285 | 3 | 279, 281, 697 |
| | 18:1/18:1 | [C$_{42}$H$_{78}$NO$_{10}$P-H]$^-$ | 786.528 | 786.529 | -1 | 290 | 288 | 2 | 281, 699 |

| | 18:0/18:1 | [C$_{42}$H$_{80}$NO$_{10}$P-H]$^-$ | 788.536 | 788.545 | -9 | 29 | 290 | 1 | 281, 283, 701 |
|---|---|---|---|---|---|---|---|---|---|
| | 18:1/20:4 | [C$_{44}$H$_{76}$NO$_{10}$P-H]$^-$ | 808.514 | 808.513 | 1 | 292 | 290 | 2 | 281, 303, 721 |
| | 18:0/20:4 | [C$_{44}$H$_{78}$NO$_{10}$P-H]$^-$ | 810.529 | 810.529 | 0 | 294 | 294 | 0 | 283, 303, 723 |
| | 18:0/20:3 | [C$_{44}$H$_{80}$NO$_{10}$P-H]$^-$ | 812.525 | 812.545 | -20 | 295 | 296 | -1 | 283, 301, 725 |
| | 18:1/20:1 | [C$_{44}$H$_{82}$NO$_{10}$P-H]$^-$ | 814.545 | 814.560 | -15 | 297 | 298 | -1 | 281, 727 |
| | 18:0/22:6 | [C$_{46}$H$_{78}$NO$_{10}$P-H]$^-$ | 834.529 | 834.529 | 0 | 298.6 | 300 | -1.4 | 283, 327, 747 |
| | 18:0/22:5 | [C$_{46}$H$_{80}$NO$_{10}$P-H]$^-$ | 836.533 | 836.545 | -12 | 300 | 302 | -2 | 283, 329, 749 |
| | 18:0/22:4 | [C$_{46}$H$_{82}$NO$_{10}$P-H]$^-$ | 838.561 | 838.560 | -1 | 301 | 303 | -2 | 283, 331, 751 |
| | 18:1/22:2 | [C$_{46}$H$_{84}$NO$_{10}$P-H]$^-$ | 840.574 | 840.576 | -2 | 302 | 305 | -3 | 281, 335, 753 |
| PI | 16:1/18:1 | [C$_{43}$H$_{79}$O$_{13}$P-H]$^-$ | 833.517 | 833.519 | -2 | 292 | 292 | 0 | 241, 253, 281 |
| | 18:1/18:1 | [C$_{45}$H$_{83}$O$_{13}$P-H]$^-$ | 861.535 | 861.550 | -15 | 300 | 300 | 0 | 241, 281 |
| | 18:0/18:0 | [C$_{45}$H$_{87}$O$_{13}$P-H]$^-$ | 865.580 | 865.581 | -1 | 304 | 303 | 1 | 241, 283 |
| | 18:1/20:4 | [C$_{47}$H$_{81}$O$_{13}$P-H]$^-$ | 883.526 | 883.534 | -8 | 306 | 306 | 0 | 241, 281, 303 |
| | 18:0/20:4 | [C$_{47}$H$_{83}$O$_{13}$P-H]$^-$ | 885.539 | 885.550 | -11 | 307 | 308 | -1 | 241, 283, 303 |
| | 18:0/20:3 | [C$_{47}$H$_{85}$O$_{13}$P-H]$^-$ | 887.553 | 887.566 | -13 | 309 | 309 | 0 | 241, 283, 305 |
| | 18:1/22:5 | [C$_{49}$H$_{83}$O$_{13}$P-H]$^-$ | 909.540 | 909.550 | -10 | 312 | 315 | -3 | 241, 281, 329 |
| | 18:1/22:4 | [C$_{49}$H$_{85}$O$_{13}$P-H]$^-$ | 911.553 | 911.566 | -13 | 313 | 317 | -4 | 241, 281, 331 |
| | 18:1/22:3 | [C$_{49}$H$_{87}$O$_{13}$P-H]$^-$ | 913.578 | 913.581 | -3 | 314 | 319 | -5 | 241, 281, 333 |

**Table S-3.** Median, range, and mean ± standard deviation (SD) values, and normality are listed for relative intensities of (**a**) ATP, (**b**) GSH, and (**c**) UDP-HexNAc in mitotic cells overall and at different mitotic stages.

| (a) ATP intensities (%) | | | | |
|---|---|---|---|---|
| **Mitotic stage (cell #)** | **Median** | **Range** | **Mean±SD** | **Normality[a]** |
| Overall (59) | 5.6 | 25.5 | 7.3±5.5 | No |
| Prometaphase (12) | 4.2 | 9.7 | 4.5±2.3 | No |
| Metaphase (14) | 6.6 | 24.8 | 9.8±8.1 | No |
| Anaphase (9) | 4.7 | 7.2 | 7.2±2.9 | Yes |
| Telophase (14) | 6.6 | 18.8 | 7.9±5.8 | Yes |
| Cytokinesis (10) | 6.5 | 14.6 | 6.5±4.0 | Yes |

| (b) GSH intensities (%) | | | | |
|---|---|---|---|---|
| **Mitotic stage (cell #)** | **Median** | **Range** | **Mean±SD** | **Normality[a]** |
| Overall (59) | 11.0 | 51.2 | 14.0±10.3 | No |
| Prometaphase (12) | 16.4 | 43.7 | 16.9±12.2 | Yes |
| Metaphase (14) | 13.0 | 50.1 | 17.7±15.0 | Yes |
| Anaphase (9) | 7.4 | 18.6 | 10.2±6.6 | No |
| Telophase (14) | 11.3 | 17.8 | 11.9±5.2 | Yes |
| Cytokinesis (10) | 12.5 | 18.3 | 11.8±6.5 | Yes |

| (c) UDP-HexNAc intensities (%) | | | | |
|---|---|---|---|---|
| **Mitotic stage (cell #)** | **Median** | **Range** | **Mean±SD** | **Normality[a]** |
| Overall (59) | 7.4 | 18.8 | 7.8±4.4 | Yes |
| Prometaphase (12) | 6.7 | 17.1 | 7.6±5.0 | Yes |
| Metaphase (14) | 4.6 | 12.8 | 5.6±3.8 | Yes |
| Anaphase (9) | 9.3 | 8.4 | 9.2±3.1 | Yes |
| Telophase (14) | 7.8 | 14.6 | 7.5±4.5 | Yes |
| Cytokinesis (10) | 8.4 | 13.5 | 10.1±4.4 | Yes |

[a]For normality testing Shapiro Wilk statistics was used.

**Table S-4.** Median, range, and mean ± SD values, and normality are listed for ratiometric indicators (**a**) AEC, (**b**) [GTP]/[GDP], and (**c**) [Hex-bis-P]/[Hex-P] in mitotic cells overall and at different mitotic stages.

**(a) AEC**

| Mitotic stage (cell #) | Median | Range | Mean±SD | Normality[a] |
|---|---|---|---|---|
| Overall (59) | 0.87 | 0.40 | 0.85±0.11 | No |
| Prometaphase (12) | 0.77 | 0.38 | 0.79±0.13 | Yes |
| Metaphase (14) | 0.93 | 0.16 | 0.92±0.06 | Yes |
| Anaphase (9) | 0.78 | 0.34 | 0.82±0.12 | Yes |
| Telophase (14) | 0.82 | 0.35 | 0.83±0.13 | Yes |
| Cytokinesis (10) | 0.87 | 0.19 | 0.87±0.06 | Yes |

**(b) [GTP]/[GDP] ratios**

| Mitotic stage (cell #) | Median | Range | Mean±SD | Normality[a] |
|---|---|---|---|---|
| Overall (42) | 1.9 | 14.5 | 2.8±2.9 | No |
| Prometaphase (10) | 0.7 | 4.8 | 1.6±1.6 | No |
| Metaphase (7) | 1.9 | 3.9 | 2.5±1.5 | Yes |
| Anaphase (8) | 1.7 | 2.5 | 1.8±1.0 | Yes |
| Telophase (10) | 1.1 | 14.5 | 3.6±4.7 | No |
| Cytokinesis (7) | 4.7 | 6.4 | 5.0±2.3 | Yes |

**(c) [Hex-bis-P]/[Hex-P] ratios**

| Mitotic stage (cell #) | Median | Range | Mean±SD | Normality[a] |
|---|---|---|---|---|
| Overall (56) | 1.4 | 8.8 | 2.0±2.0 | No |
| Prometaphase (12) | 0.6 | 5.0 | 1.4±1.6 | No |
| Metaphase (12) | 1.1 | 8.6 | 2.0±2.5 | No |
| Anaphase (9) | 1.8 | 6.9 | 2.7±2.5 | Yes |
| Telophase (13) | 1.5 | 7.3 | 2.2±1.9 | No |
| Cytokinesis (10) | 1.5 | 3.0 | 1.7±1.1 | Yes |

[a]For normality testing Shapiro Wilk statistics was used.

**Table S-5.** Statistically significant ($p < 0.05$) correlations with $r_{ij} > 0.55$ between ions and ionic fragments observed in overall mitotic cell population (n = 59).

| Metabolite 1 | | Metabolite 2 | | | |
|---|---|---|---|---|---|
| *m/z* | **Assignment** | *m/z* | **Assignment** | $r_{ij}$ | **-log ($p$)** |
| 130.085 | leucine/isoleucine | 145.059 | glutamine | 0.83 | >15.0 |
| 130.085 | leucine/isoleucine | 146.044 | glutamate | 0.57 | 5.5 |
| 145.059 | glutamine | 146.044 | glutamate | 0.61 | 6.5 |
| 191.015 | citric acid | 254.077 | GSH fragment | 0.67 | 8.1 |
| 210.086 | GSH fragment | 338.065 | S-sulfanylglutathione | 0.57 | 5.6 |
| 346.056 | AMP | 362.048 | GMP | 0.69 | 8.9 |
| 402.995 | UDP | 426.022 | ADP | 0.77 | 12.1 |
| 402.995 | UDP | 442.015 | GDP | 0.64 | 7.3 |
| 426.022 | ADP | 442.015 | GDP | 0.66 | 7.8 |
| 481.975 | CTP | 482.961 | UTP | 0.67 | 8.3 |
| 481.975 | CTP | 521.982 | GTP | 0.65 | 2.1 |
| 482.961 | UTP | 505.987 | ATP | 0.64 | 7.4 |
| 482.961 | UTP | 521.982 | GTP | 0.62 | 6.7 |
| 505.987 | ATP | 521.982 | GTP | 0.71 | 9.6 |
| 494.047 | UDP-HexNAc fragment | 522.041 | UDP-hexose fragment | 0.94 | >15.0 |
| 494.047 | UDP-HexNAc fragment | 563.067 | UDP-HexNAc fragment | 0.93 | >15.0 |
| 522.041 | UDP-hexose fragment | 563.067 | UDP-HexNAc fragment | 0.91 | >15.0 |
| 565.049 | UDP-hexose | 606.074 | UDP-HexNAc | 0.89 | >15.0 |

**REFERENCES**

(1) Zieve, G. W.; Turnbull, D.; Mullins, J. M.; McIntosh, J. R. *Exp. Cell Res.* **1980**, *126*, 397-405.

(2) Mejillano, M. R.; Shivanna, B. D.; Himes, R. H. *Arch. Biochem. Biophys.* **1996**, *336*, 130-138.

(3) Akhmanova, A.; Steinmetz, M. O. *Nat. Rev. Mol. Cell Biol.* **2008**, *9*, 309-322.

(4) Akhmanova, A.; Steinmetz, M. O. *Nat. Rev. Mol. Cell Biol.* **2015**, *16*, 711-726.

(5) Hendzel, M. J.; Wei, Y.; Mancini, M. A.; VanHooser, A.; Ranalli, T.; Brinkley, B. R.; BazettJones, D. P.; Allis, C. D. *Chromosoma* **1997**, *106*, 348-360.

(6) Xu, Y. F.; Lu, W. Y.; Rabinowitz, J. D. *Anal. Chem.* **2015**, *87*, 2273-2281.

(7) Park, J. O.; Rubin, S. A.; Xu, Y. F.; Amador-Noguez, D.; Fan, J.; Shlomi, T.; Rabinowitz, J. D. *Nat. Chem. Biol.* **2016**, *12*, 482-489.

(8) Paglia, G.; Williams, J. P.; Menikarachchi, L.; Thompson, J. W.; Tyldesley-Worster, R.; Halldorsson, S.; Rolfsson, O.; Moseley, A.; Grant, D.; Langridge, J.; Palsson, B. O.; Astarita, G. *Anal. Chem.* **2014**, *86*, 3985-3993.

(9) Paglia, G.; Kliman, M.; Claude, E.; Geromanos, S.; Astarita, G. *Anal. Bioanal. Chem.* **2015**, *407*, 4995-5007.